ABSTRACT

Title of Thesis: MECHANICAL MAPPING OF NEURAL TUBE CLOSURE IN LIVE EMBRYOS USING BRILLOUIN MICROSCOPY

Chenchen Handler, Master of Science, 2022

Dissertation directed by: Professor Giuliano Scarcelli,
Department of Bioengineering

Neurulation is a process that serves as the precursor to the spinal cord in vertebrates. Neural tube closure (NTC), part of primary neurulation, involves the extensive coordination of cellular, molecular, and mechanical events to transform the flat neural epithelium to a luminated epithelial tube. Neural tube defects (NTD) are the result of mechanical failures that arise during neurulation. Recent research has focused on understanding the molecular mechanisms underlying neurulation but has difficulty correlating them to physical mechanisms. To better understand how physical mechanisms are integrated and responsible for neurulation, several techniques have been applied to study NTC in a range of *in vitro* environments. However, many of these techniques have been limited due requiring the specimen to be fixed and/ or being invasive and requiring physical contact with the specimen to extract the modulus. As such, there is limited resolution and only the superficial layer of the sample is measured making assessing 2D/3D tissue mechanics inside a

growing organism is highly challenging. In this dissertation, we aim to quantify the mechanical state of the neural tube without disruption to development. To do this, we adapted Brillouin microscopy, a non-invasive, label- and contact-free imaging technique, to allows us to probe the longitudinal modulus of the neural plate at every step of NTC with cellular resolution. This quantification is performed as the embryo develops in real time using time-lapse Brillouin and an improved *ex-ovo* culture method. We observed an increase in the Brillouin modulus of the neural plate as the embryo develops from Hamburger-Hamilton stage (HH)-6 to HH-12. This increase in modulus is consistent with previous data from other vertebrates such as Xenopus and Mouse embryos and demonstrates the process of neurulation is driven by mechanical forces. Time-lapse Brillouin imaging depicted stiffening and thickening of the neural plate during NTC, suggesting these are coordinated events for NTC. Here, we show that tissue stiffness plays an integral role in NTC and directly quantifying tissue mechanics during neurulation should allow us to better determine the biomechanical nature of NTD.

MECHANICAL MAPPING OF NEURAL TUBE CLOSURE IN LIVE EMBRYOS USING BRILLOUIN MICROSCOPY

by

Chenchen Handler

Thesis submitted to the Faculty of the Graduate school of the
University of Maryland, College Park, in partial fulfillment
of the requirements for the degree of
Master of Science
2022

Advisory committee:
Professor Giuliano Scarcelli, Chair
Professor Huang Chiao Huang
Professor Jitao Zhang

Acknowledgements

This work has been made possible with the help, contribution, and effort of several people who have supported me during my time at the University of Maryland. Above anyone else, I would like to thank Jitao Zhang and Giuliano Scarcelli for taking a chance on me as a second-year undergraduate who, on a whim, applied for a position within Giuliano's lab. Their commitment to me as mentors has paved the path for my scientific work and approach to scientific knowledge.

I would also like to thank Miloš, for the great guidance, mentoring, fun discussions, and support. Thanks to my fellow colleagues Justin, Jake, Giulia, Raymundo, Romanus, Eric, Maggie, Lydia, and Christina for their discussion and friendship. I thank my parents, Changge and Stephen, who continuously supported and encouraged me to explore all that I can.

Finally, I would like to thank my committee for taking the time to advise me and read this work. Along with them all faculty and staff of the Fischell Department, the University of Maryland undergraduate and graduate school. I am extremely grateful to be a Bioengineering Terp.

Table of Contents

List of figures

1. Neurulation and Brillouin Microscopy

1.1. Introduction

Neurulation is a key process in early gestational development of the brain and spinal cord. Neural tube closure (NTC) is a central procedure of vertebrate neurulation where the planar neural plate will be elevated and fused to form a hollow neural tube. A failure of this procedure can result in severe neural tube defects (NTD), which represent one of the most common human birth defects (Wallingford et al., 2013). Genetic and molecular processes that guide NTC have been extensively studied for many decades (Colas and Schoenwolf, 2001; Copp et al., 2003; Wilde et al., 2014). On the other hand, biomechanical mechanisms that may be involved in NTCs are attracting increasing attention in recent years (Koehl, 1990; Schoenwolf and Smith, 1990; Vijayraghavan and Davidson, 2017). On cell and tissue level, the morphogenesis of neural tube (NT) can be considered as a result of the interaction between the generated force and the mechanical resistance of the embryonic tissue (Heer and Martin, 2017; Nikolopoulou et al., 2017): the successful closure of NT requires the intrinsic force can overcome the opposing tissue tension that relies on its elastic property. As such, the alteration of tissue biomechanics can cause the failure of the closure and thus malformation of NT (Galea et al., 2017). Although the force production and tissue stiffening during the procedure of NTC have been observed in experiments (Zhou et al., 2009, 2015; Galea et al., 2017), the quantitative contribution of specific biomechanical processes to ensure robust neurulation remains mostly unknown. One of the main reasons is the lack of tools that can map the biomechanics of neural plate tissue *in situ* and in real time when the embryo is developing.

Confocal Brillouin microscopy is an emerging technique for quantifying the mechanical properties of biological materials (Scarcelli et al., 2015; Prevedel et al., 2019; Zhang and Scarcelli, 2021). Different from conventional mechanical test methods, Brillouin microscopy uses a single

laser beam to measure the elastic properties of the material. This is based on an optical phenomenon called spontaneous Brillouin light scattering (Boyd, 2003), where the interaction of the incident laser beam and the acoustic phonon within the material will introduce a frequency shift (Brillouin shift) to the scattered light (see Material and methods). By measuring the Brillouin shift of the scattered light using a self-built spectrometer, the elastic longitudinal modulus of the material can be directly quantified. Since Brillouin microscope is designed in a confocal configuration, it can achieve diffraction-limited spatial resolution. In the past several years, we have innovated this technique and demonstrated its feasibility for quantifying the mechanical properties of single cell (Wisniewski et al., 2020; Zhang et al., 2020), embryonic tissue (Raghunathan et al., 2017), and neural plate (Zhang et al., 2019) with subcellular resolution and enough mechanical sensitivity. As an all-optical technique, Brillouin microscope can conduct measurement in a non-contact, non-invasive, and label-free manner. Therefore, it could be a promising tool for mechanically mapping the neural plate tissue *in situ* during embryonic development.

1.2. Neural tube closure

The brain and spinal cord of vertebrates begin with the formation of a tube. There are slight variations in primary neurulation between animal groups. For example, in amphibians, closure occurs almost simultaneously at all axial levels. In mammals and avian animals, neurulation events occur sequentially at multiple sites following a progressive closure style like a zipper (Davidson and Keller, 1999; Nishimura et al., 2012; Spear and Erickson, 2012; Nikolopoulou et al., 2017). In chick embryos, neurulation has two points of closure initiation at the future midbrain and at the

caudal hindbrain/cervical boundary, and bidirectional zippering occurs between the sites (Figure 1) (Van Straaten et al., 1996; Nikolopoulou et al., 2017).

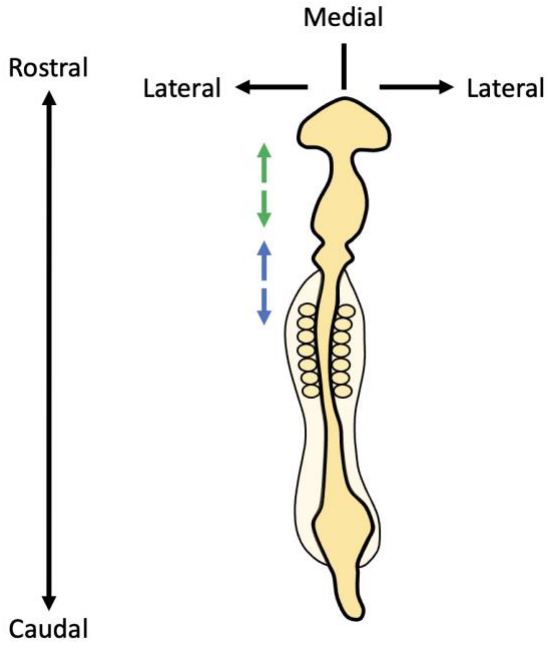

Figure 1. Schematic of closure points in chick embryo from a dorsal view with axial identification. Green arrows refer to midbrain closure point and blue arrows refer to the hindbrain/cervical boundary midpoint. Arrow directions indicate bidirectional closure, zippering, at each closure point.

The NP is initially identified as a flat sheet of neuroepithelial cells referred to as the neural ectoderm (NE). The surrounding tissue include: the non-neural ectoderm (NNE), bordering the NE, the mesoderm, and notochord (Wilde et al., 2014) (Figure 2A). The initiation of NTC begins with the shaping of the NP whereby the NP thickens in the dorsal-ventral axis (perpendicular to the medial-lateral axis) and is accompanied by the apical-basal heigh increase in NE cells. Concurrently, a process called convergent extension (CE) act on the lateral edges of the NP causing convergence towards the dorsal midline while elongating the NE in the anterior-

posterior (rostro-caudal) direction. Mediolateral cell intercalation drives CE and the shaping process (Nishimura et al., 2012; Williams et al., 2014). During CE, cells converge by intercalating perpendicular to the extension axis. This creates an array of cells that is longer (extension) but thinner (convergence).

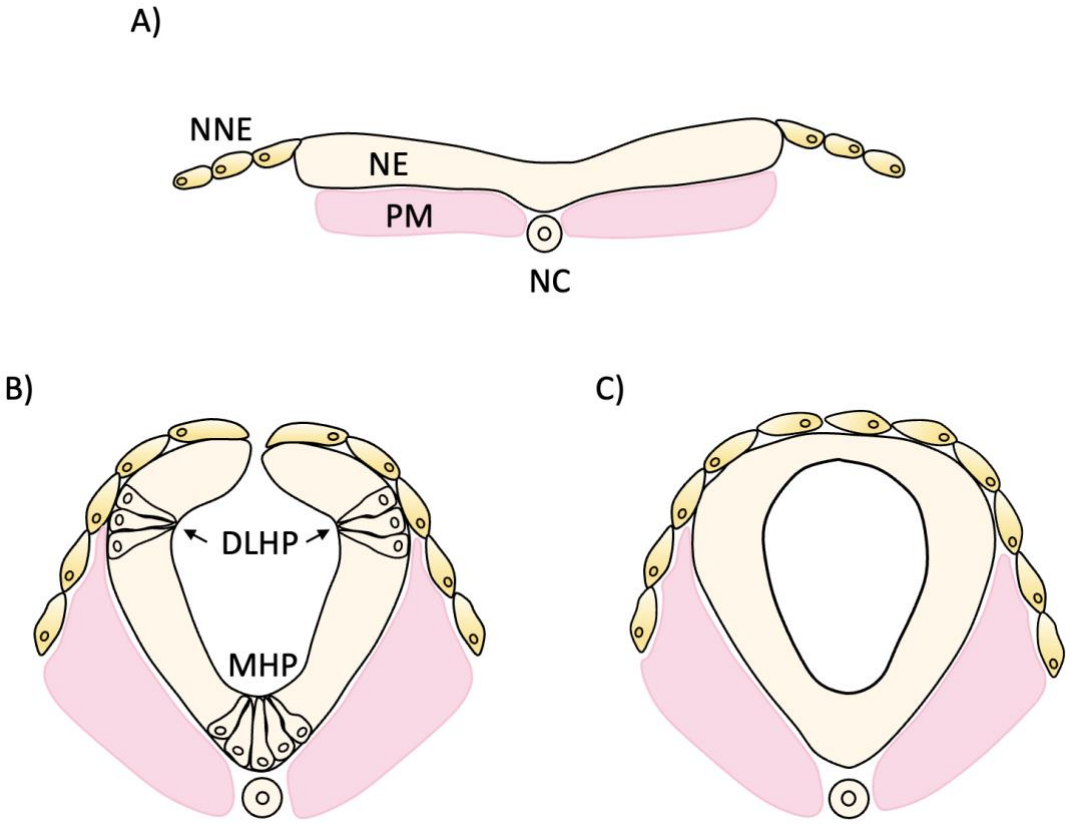

Figure 2. General overview of primary neurulation. A) Flat neural ectoderm (NE) surrounded by non-neural epithelium (NNE), paraxial mesoderm (PM), and the notochord (NC). B) Elevation of the neural folds is followed by formation of the mediolateral hinge point (MHP), and formation of the dorsolateral hinge points identified by the wedge-shaped NE cells. C) Fusion of the neural folds result in formation of the NT beneath a layer of NNE.

Next comes NP bending when the median hinge point (MPH) forms at the dorsal midline (Figure 2B). The MHP is identified by wedge-shaped cells, caused by apical constriction,

adjacent to non-constricted cells (Schroeder, 1970). The lateral edges of the NP is elevated due to the constriction of cells at the MHP, creating the neural folds (Morita et al., 2012). Throughout the bending process, the NP continues to converge and extend and guide the neural folds towards apposition. The dorsolateral hinge points (DLHP) are formed between the medial and lateral margins (Figure 2B) of the NP to assist fold apposition. The two ends are now referred to as the neural crest. The timing and location of the formation of DHP varies between species. When the neural folds are apposed, remodeling of the NE and the NNE occurs to form a closed NT covered by a single layer of NNE (Wilde et al., 2014; Vijayraghavan and Davidson, 2017) (Figure 2C). Once the NT is formed, the neural crest is disconnected from the ectoderm. The neural crest cells will differentiation and form most of the peripheral nervous system (Chhetri and Das, 2021).

As one might expect, this highly orchestrated process is sensitive to perturbations which, in all vertebrates, can result in NTD which affect approximately one in every 1000 births (Lozano et al., 2012; Mai et al., 2014; Copp et al., 2015, p. 2015; Morris et al., 2016). Failure of closure in the spinal region can lead to a variety of NTDs, most commonly spina bifida and most severe being myelomeningocele, (severe form of spina bifida) and results in increased risk of mortality with those who survive facing life-long disabilities and complications. More severely, cranial NTD during primary neurulation leads to death before birth.

1.3. Neurulation biomechanics

The process of primary neurulation in vertebrates is a complex morphogenetic process involving the coordination of multiple cellular and molecular events along with mechanical tissue movements that remodels the flat neural plate (NP) into the lumenized NT (Davidson, 2012; Wilde et al., 2014). Efforts in researching the cellular, molecular, and genetic processes during

neurulation has successfully resulted in identifying biological events and pathways essential to neurulation and genes associated with NTD. However, it has been difficult to associate the molecular mechanisms to the physical mechanisms that drive NTC. This chapter will illustrate the physical mechanics of neurulation and how NTC arise from mechanical failures.

As discussed previously, neurulation occurs in four sequential stages. The closure process is initiated when the NP undergoes differentiation, then bending – hinge-point formation and establishing the neural folds, followed by elevation towards the dorsal midline, and finally complete when the tips of the neural folds fuse together (Ray and Niswander, 2012). From shaping to fusion to the propagation of NTC along the body axis, cellular processes drive biomechanical events at every step. In parallel, biomechanical forces provide feedback to cells, influence gene expression, modulate cell shape, and designate proliferation and survival.

Originally, it was thought that extrinsic forces from the epidermal tissue surrounding the edges of the NP could drive neural plate invagination (His, 1874) but the theory lost favor when it was shown that folds still formed even when isolated from surrounding tissues (Roux, 1885). It would not be until 30 years later that embryologists proposed more intrinsic mechanisms such as apically constricting cells in order to generate enough tension and force to drive folding (Glaser, 1916; Lewis, 1947). Imaging with electron microscopy revealed cytoskeleton elements and intracellular vesicles which were associated with cell shape change and aided in NP deformation during NTC (Baker and Schroeder, 1967; Karfunkel, 1971, 1972; Brun and Garson, 1983; Schoenwolf and Powers, 1987). While experimental models enabled the identification of several molecular regulators of apical constriction (Sawyer et al., 2010), others have suggested alternative and parallel mechanisms that also drive bending (Davidson et al., 1995). The NC and other dorsal tissues including the paraxial somitic mesoderm (PM) are thought to contribute to dorsal extension.

The NC acts as a growth factor release center and a mechanical structure, functioning as a stiff backbone in tadpoles (Wassersug, 1989; Hoff and Wassersug, 2000). Experiments in which the NC was ablated, both amphibian (Kitchin, 1949) and zebrafish (Talbot et al., 1995) embryos were shown to have shortened axes resulting in failure of dorsal tissue elongation. These studies suggest the dorsal mesodermal tissues play an important mechanical role during NTC by applying forces to the neural plate, extend the dorsal axis, and closing the NT. However, in a later study, it was found that by isolating the paraxial tissues adjacent to the NT revealed that the PM was responsible for more than 60% of the mechanical stiffness of the dorsal axis rather than the NT (Zhou et al., 2009). The origin of the mechanical stiffness is still highly debated as several components such as Collagen type II fibers (Levental et al., 2007), fibronectin (Lee et al., 1984), fibrillin (Waters et al., 2002; Skoglund et al., 2006), laminin (Wedlich et al., 1989), and other factors such as actomyosin cytoskeleton (Kofron et al., 2002; Tao et al., 2007) are identified as potential stiffness contributors but little is understood about how they contribute to the mechanical properties of tissue. Studies have tried to isolate certain components of force contribution by performing knock down assays and subsequently measuring the stiffness of the tissue. However, results from different experiments may not often agree (Davidson et al., 2006; Zhou et al., 2009). Due to these different approaches, the contributions of force generation from physical mechanisms during NTC still requires more extensive understanding.

Multiple experiments have demonstrated that extrinsic forces can prevent NTC, implying that intrinsically generated forces are necessary to achieve closure. In chick embryos, by culturing on curved substrates and therefore introducing changes to the tissue curvature can delay spinal closure. Suggesting that NTC can be modulated based on extrinsic mechanical forces applied to the closing NP (van Straaten et al., 1993). Other studies performed have tried to capture the *in vivo*

forces produced during NTC by quantifying the expansion of incisions in different tissues. In amphibians, small incisions in the ectoderm (NNE) extend uniformly and rapidly in all directions suggesting the ectoderm's ability to withstand isotropic stresses. In axolotl embryos, microsurgical slit expansion demonstrates isotropic stresses in the epidermis but anisotropic stresses in the neuroepithelium (Benko and Brodland, 2007) indicating internal pressures that drive neurulation.

While these studies show that extrinsic forces can perturb the biomechanical events driven by intrinsically generated forces. Still, little is known about the extent of the contribution of specific biomechanical processes that ensures robust neurulation. As discussed earlier, the association between molecular and physical mechanisms is lacking and the mechanical description of neurulation is necessary to understand the origins of NTD. As all neural tube defects are mechanical in nature and understanding neurulation mechanics should allow us to better associate specific cellular sources that contribute to defects in tissue mechanical properties, force generation, or patterning.

1.4. Methods for measuring neural tube mechanics

Many important techniques have been developed to quantify the mechanical properties of embryonic tissue (Campas, 2016), which can be approximately classified into three categories: contact-based methods, bead/droplet-based sensors, and tissue ablation/dissection.

Contact-based techniques include atomic force microscopy (AFM) (Franze, 2011; Barriga et al., 2018) or microcantilever (Zhou et al., 2009; Chevalier et al., 2016; Marrese et al., 2019) based indentations, micropipette aspiration (Wen et al., 2015), and tensile tests (Wiebe and Brodland, 2005). AFM and other cantilever-based methods utilize a tipped cantilever to approach the sample from above. By indenting the sample, 2D surface measurements of Young's modulus,

adhesion force, and deformation can be obtained. Micromanipulations using glass needles are used to load tissue with tensional forces which can be modulated by controlling the duration and amount of force/pressure applied. This technique allows one to observe how the sample reacts to the aspirational forces. For tensile tests, wires may be fixed to the sample and separated at a constant strain rate to determine the resultant stress. While the contact-based techniques can provide direct quantification of tissue's elastic modulus, they need physical access of the sample and to apply force to deform the sample during measurement. Since neural tube tissue has irregular shape in 3D and mechanically interconnected, isolate explants are usually required for unambiguous mechanical test.

Bead/droplet-based sensors include optical/magnetic tweezer (Welte et al., 1998; Savin et al., 2011) and microdroplet (Campàs et al., 2014). Optical/magnetic tweezer uses force-driven rigid beads or droplets to sense the mechanical properties of localized tissue. A highly focused laser beam can move the refractile particles to exert and measure forces. Microdroplet uses deformable droplet to quantify the tissue stress by analyzing the shape of the droplet via fluorescence microscopy. These sensors can quantitatively measure the mechanical properties with subcellular resolution after careful calibration. However, they require injection of beads or droplets into tissue, making them invasive and low throughput.

Tissue ablation/dissection uses either an ultrafast pulsed laser beam (Galea et al., 2017) or a blade (Beloussov et al., 1975) to dissect a portion of the tissue and evaluate the mechanical properties based on the relaxation response. This method provides a semi-quantitative platform to understand the stresses within tissue sheets. One can accurately control where cuts are made and the initial recoil within the first few seconds describes the local and directional strains within the tissue. This is an attractive technique because of the simple setup. Due to the mechanical

connection of embryonic tissue in 3D, this method mostly provides global assessment on relatively large scale.

To summarize, existing methods have greatly advanced the assessment of embryonic tissue biomechanics. However, due to the technical limitations, the *in situ* mechanical mapping of the neural plate tissue during the procedure of NTC in live embryo has not been reported.

1.5. Biomechanics measurements via Brillouin scattering

1.5.1. Brillouin scattering

Brillouin light scattering (BLS) is based on inelastic scattering of light due to variations in the dielectric constant in a material with the most common ones being vibrational or magnetic oscillations (Fiore, 2021). This portion of the thesis will focus on vibrational oscillations (phonons) which are characterized as vibrational modes of collective pressure waves within a material. This thesis will also focus on spontaneous Brillouin scattering where the acoustic phonons are generated by spontaneous thermal fluctuations within a material while in thermodynamic equilibrium and without external perturbations. Like Raman scattering, Brillouin scatters light off vibrational modes and the frequency of the incident light is changed during the scattering event. However, Raman scattering is the result of molecular rotation and vibrational transitions whereas BLS is the result of scattered light from acoustic phonons.

Consider the frequency ω of scattered light from an object, we must first consider the incoming wavevector, $\overrightarrow{k_i}$ with frequency ω_i, and the scattered light wavevector $\overrightarrow{k_s}$ with frequency ω_s. The subsequent wavevector transfer is described as

$$\vec{q} = \overrightarrow{k_s} - \overrightarrow{k_i} \tag{1}$$

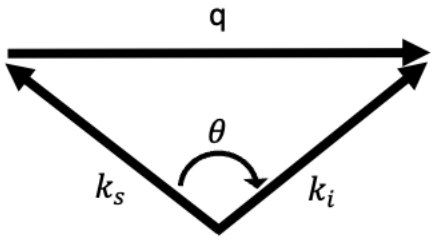

Figure 3. Schematic of scattering process.

Wavevectors are assumed to not be parallel, thus θ is defined as the angle between $\overrightarrow{k_i}$ and $\overrightarrow{k_s}$ and vector $\vec{q}$ points in the direction of the traveling sound wave (Figure 3).

Depending on the frequency of the incident light ω_i, the resulting scattered light, ω_s, will experience an upward and downward propagation

$$\omega_s = \omega_i \pm \Omega \tag{2}$$

where Ω represents the frequency of the thermal pressure waves.

Thermal acoustic phonons are related to the local mechanical properties of a material and travel at the speed of sound, v_s

$$v_s = \sqrt{\frac{M'}{\rho}} \tag{3}$$

where M represents the longitudinal elastic modulus of the material and ρ represents the mass density. In addition, the acoustic waves have a dispersion relationship where $\Omega = qv_s$ so eq (3) can be rewritten as

$$\Omega = \sqrt{\frac{M'}{\rho}} \cdot q \tag{4}$$

Since the typical frequency shift of the phonon is very small (GHz regime) compared to the frequency shift of photons (THz regime), we can approximate $k_i \cong k_s$ and the wavevector transfer intensity, q, can be written as

$$q = 2nk \cdot \sin\frac{\theta}{2} = \frac{4\pi n}{\lambda} \cdot \sin\frac{\theta}{2} \tag{5}$$

Finally, we obtain an expression for the Brillouin frequency shift ω_B, written as

$$\Omega = \omega_B = \frac{2n}{\lambda} \cdot \sqrt{\frac{M'}{\rho}} \cdot \sin\frac{\theta}{2} \tag{6}$$

where n is refractive index of the material, λ is the laser wavelength, M' is the longitudinal modulus that quantifies the mechanical property, ρ is the density, and θ is the collection angle of the scattered light. In our Brillouin microscope, backward scattered light was collected, yielding $\theta = 180\,°$. The Brillouin spectrum of scattered light contains a central elastically scattered light component and the Brillouin double peaks (Figure 4) sometimes referred to as the Brillouin triplet.

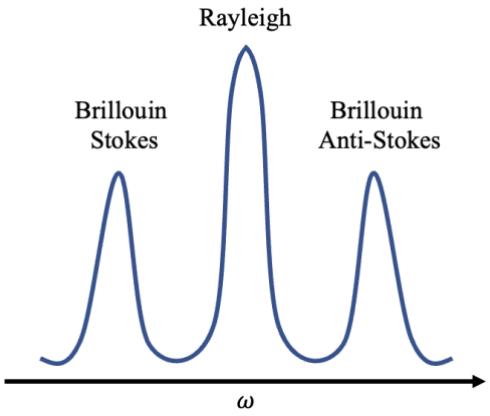

Figure 4. Brillouin spectrum with both inelastically scattered Stokes and Anti-Stokes frequencies centered around the elastically scattered Rayleigh peak. The Stokes component has lower energy while the Anti-Stokes component contains higher energy photons compared to the incident photon.

Based on previously published data, the ratio of refractive index and density $\rho/_{n^2}$ is assumed to be constant within a given biological material (Scarcelli et al., 2011, 2012, 2013, 2015; Kim and Guck, 2020). Thus, we can assume that the Brillouin frequency shift has a one-to-one relationship to the longitudinal modulus where $\Omega \propto \sqrt{M'}$. In this dissertation, the reported Brillouin shift values are in GHz, representative of the measure of the mechanical properties in embryonic tissue. The timescale of Brillouin microscopy is determined by the characteristic frequency of the phonons in the material, here it is on the timescale of 1-10 GHz. The length scale, determined by the order of the wavelengths of phonons (on the order of hundreds of nanometers), is when Brillouin interactions occur and Brillouin scattering probes the mechanical properties of the material.

1.5.2. Longitudinal modulus

Brillouin light scattering (BLS) was discovered in 1922 (Brillouin, 1922) and initially used to characterizing condensed matter in solid-state physics, crystallography, and geology. For these

materials, Brillouin can directly measure the full elastic tensor and the mechanical interpretation is straightforward. It was not until the late 1970s-early 1980s that BLS was used to investigate biological samples (Randall et al., 1979). However, in biological tissues, which do not follow the straightforward rules of elastic solids, there is more complexity relating longitudinal modulus with other moduli.

Elastic modulus consists of the stress and strain that describe the material properties of objects. Stress is defined as force acting over an area and strain is an unitless measure of the changes along a dimension of a deformable body, both of which are volume-averaged tensors (Humphrey, 2001). Depending on the orientation of stress applied, specific strains can be measured. The various elastic moduli are quantified by the experimental configuration of the geometry of stress and strain of an object (Figure 5). The relationship between longitudinal

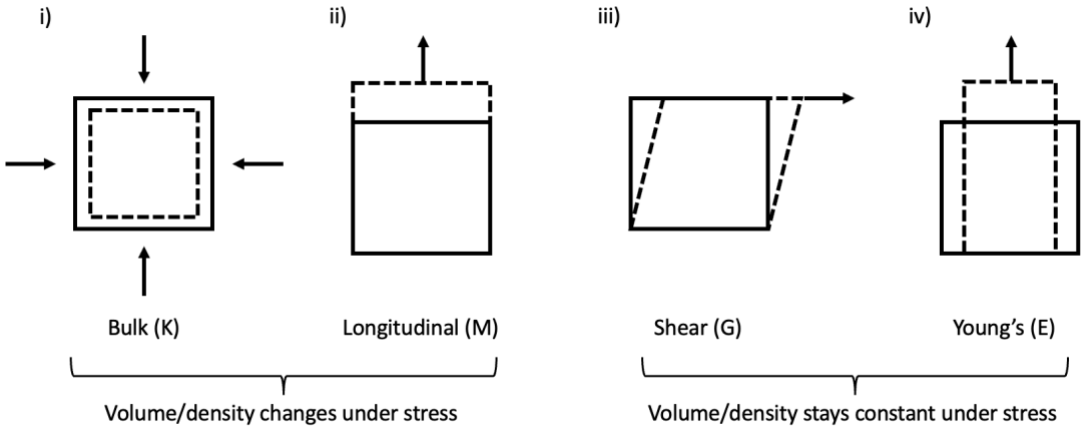

Figure 5. Illustration of the main tress-strain relationships in mechanobiology. i) Bulk (K) and ii) longitudinal (M) moduli are associated with deformation changes in volume under stress. iii) Shear (G) and iv) Young's (E) moduli are associated with volume-conserving deformation under stress. M and K describe a uniaxial stress-strain relationship.

modulus and the other mechanical moduli in elastic solids are well established (Scarcelli et al., 2011, 2015). Longitudinal modulus is similar to Young's modulus in that they both describe a uniaxial stress-strain relationship. The key difference remains in that the object deforms perpendicular to the direction of applied stress under Young's modulus while longitudinal modulus probes the ratio of uniaxial stress-strain in a confined condition (Prevedel et al., 2019).

Tissues have high water-content and exhibit near incompressibility which results in a significantly lower shear modulus compared to the bulk modulus (G << B). In highly hydrated materials, the bulk modulus of water dominates and results in the longitudinal modulus measured by Brillouin spectroscopy to be higher (GPa regime) compared to typical shear or Young's moduli (Pa – kPa regime) measured in tissues (Nikolić, 2022). The elastic constant in biological materials is also dependent on the frequency of the periodically applied stress which can either be low frequency and high frequency. Traditional mechanical rheometers perform quasi-static viscoelastic measurements while in Brillouin measurements, the modulus is probed at high frequency on the order of 10^{10} Hz. It has been empirically shown that Brillouin measured longitudinal modulus, M', has a log-log linear relationship to the quasi-static Young's (or shear) moduli, E':

$$\log M' = a \log E' + b \tag{7}$$

Where a and b are material-dependent coefficients and range between 0.02 – 0.1 in biological materials. From this log-log relationship, the relative change of Brillouin modulus is related to the relative change in Young's modulus (Scarcelli et al., 2011, 2015):

$$\frac{\Delta M'}{M'} = a \cdot \frac{\Delta E}{E} \tag{8}$$

The relative error calculated for the frequency sensitivity of the Brillouin microscope is $\Delta M'/_M = 0.02\%$ and corresponds to the sensitivity of 2-10% in Young's modulus. The power-law scaling of elastic moduli dependent on frequency has also been shown in cells, tissues, and cytoskeleton (Duck, 1990; Fabry et al., 2001). Even so, the relationship between longitudinal modulus measured in tissues and quasi-static Young's modulus requires a more thorough interpretation and understanding.

1.5.3. Brillouin spectroscopy

The Brillouin signal collected from back scattered light is shifted on the order of GHz which corresponds to approximately several picometers in wavelength. Due to the inefficiency of the spontaneous BLS process (1 photon in a billion) and the narrow range of frequencies necessary for detection (Prevedel et al., 2019), common grating or prism spectrometers would not have sufficient throughput and spectral resolution. The Fabry-Perot interferometer (FPI) is the original spectroscopic technique implemented in Brillouin and first proposed in 1897 (Fabry and Perot, 1897). A FPI consists of a set of two parallel mirrors separated by a free space of a specific length, also known as the Fabry-Perot etalon, and light can either travel through or be reflected by the instrument depending on the distance between the mirrors (Mielke and Elam, 2009). The constructive interference condition is described by $m\lambda = 2 \cdot d \cdot cos\theta$. The position of the mirrors determines the type of interference (constructive or destructive) generated and what parts of the Brillouin spectrum is being scanned. A standard FPI uses one etalon and has the resolution of a few tens of megahertz. While this setup provides high resolution, there is not enough spectral contrast to distinguish the Brillouin signal. To increase the spectral contrast, two FPIs are coupled together, known as a Tandem Fabry-Perot interferometer (TFPI). For a multi-pass TFPI, scattered light passes through the two cavities three times for a total of six passes. By combining the spectral

contrast of all the etalon passes, a TFPI can achieve up to 100 dB of spectral contrast. Thus, TFPIs became a standard in Brillouin spectroscopy and was used for a variety of applications such as material characterization (Dil, 1982) and some mechanobiological probing (Randall et al., 1979; Lee et al., 1987; Lees et al., 1990). However, the drawbacks of a TFPI system are due to loss of light in the reflected interference pattern. For this reason, TFPI-based Brillouin research in biology has been limited due to the long acquisition times (more 10 seconds per pixel) as acquisition of spectral components occur in a sequential manner and at low-throughput. While acceptable for single point/ low sampling point measurements, TFPIs is not suitable for live cell imaging which consists of high sampling points and scanning in three-dimensional volumes.

To utilize Brillouin for biological applications, Virtually Imaged Phased Array (VIPA) interferometers were introduced in 2008 (Scarcelli and Yun, 2008). A VIPA's design consists of a glass etalon, like a FP, but with a highly reflective coating (>99.9%) on the first surface along with a thin strip that has anti-reflection coating. This strip is where the cylindrical lens will send the incoming laser light into. The VIPA's second surface has a partially reflecting coating (~95%) which allows the light to pass through. The dispersed light is captured by a CCD after a focusing lens outputting a central Rayleigh scattered peak and both the Brillouin Stokes and anti-Stokes scattered peaks (Scarcelli and Yun, 2008). VIPA based spectrometers enabled fast acquisition of Brillouin spectra due to the ability to acquire all spectral components at high throughput compared to an FPI. This improved acquisition time is not without tradeoffs. The resolution of VIPA spectrometers is in the order of 0.5 GHz so the measurement of the Brillouin frequency shift is straightforward, but the measurement of the linewidth requires further processing. The contrast of a single VIPA etalon is only 30dB which can only measure nearly

transparent samples (Scarcelli et al., 2008). For these reasons, over the past 10 years, VIPA spectrometers have been designed in multi-stage architectures.

In 2011, the multi-stage cross-axis configuration was introduced. This approach allows stray light to be separated and filtered from the spectra signal which greatly reduces the background and crosstalk. With two stages, the extinction is improved to 55 dB (Scarcelli et al., 2011). Even greater extinction can be achieved with an additional third VIPA stage (~80 dB) but at a significant insertion loss. Further enhancements came from apodization which brought the spectral extinction to 70 dB (Scarcelli et al., 2015). Even so, Brillouin spectral measurements were still limited in highly scattering media. By integrating spectral coronography within a double stage VIPA spectrometer, background noise can be reduced with no insertion loss. This method yields up to an additional 20 dB in spectral extinction (Edrei et al., 2017), allowing the system to reach ~80 dB. At high-extinction (80 dB), the elastic background is effectively suppressed and the measurements are shot-noise limited in biological tissues (Fiore et al., 2016). Currently, our lab has built the fastest Brillouin spectrometer (~20 ms), coupled to a confocal microscope, that can perform sub-micron imaging in biological samples.

2. Mechanical Mapping of Neural Tube Closure in Live Embryos Using Brillouin Microscopy

2.1. Introduction

The biomechanical changes that occur during the formation of the neural tube, or neurulation, are known to regulate and drive NTC. Neurulation occurs in four stages: formation, shaping, bending, and closure, which gives way to the spinal cord in vertebrates (Ray and Niswander, 2012). While the genetics of the development process has been extensively studied, the mechanics that drive neural tube formation in early embryonic development remains mostly unknown. Failure of NTC can result in severe congenital malformations (Mai et al., 2014; Copp et al., 2015; Morris et al., 2016) and as a result, it is necessary to study the timing and the extent of the mechanical effect these cellular and molecular components induce during neurulation. Current techniques such as atomic force microscopy (Franze, 2011; Barriga et al., 2018) and fiber-based cantilever (Zhou et al., 2009; Chevalier et al., 2016; Marrese et al., 2019) require the specimen to be fixed and require physical contact to extract the elastic modulus. As such, extensive tissue preparation is required along with a limited field of view, making the assessment of 2D/3D tissue mechanics inside a growing organism is highly challenging.

In this work, we investigated the mechanical changes of the NP from formation to closure within intact live chick embryos. Using Brillouin microscopy, we were able to quantify the longitudinal modulus of the NP with cellular resolution in real time as the embryo develops (time-lapse Brillouin imaging) in a non-invasive, contact-, and label-free way. To do this, we improved the *ex-ovo* culture method which allows us to map the neural plate while the embryo continues to develop outside of their native environment. Directly quantifying tissue mechanics

in developing embryos potentially paves the way to better understand how cellular and molecular behaviors regulate the biomechanics underlying NTC.

2.2. Brillouin Instrumentation

Brillouin spectrometers can be configured with an inverted confocal microscope as a possible experimental setup (Figure 6). Compatible with lasers of any visible wavelength, we deploy a 660 nm Nd:YAG lasers for its narrow linewidth and stability. An objective lens both focuses the laser light onto the sample and act as the collector lens for backscattered laser light. Here, the scattering angle $\theta = 180°$ and the Brillouin frequency ω_B from eq (9) can be rewritten as

$$\omega_B = \frac{2n}{\lambda} \cdot \sqrt{\frac{M'}{\rho}} \tag{9}$$

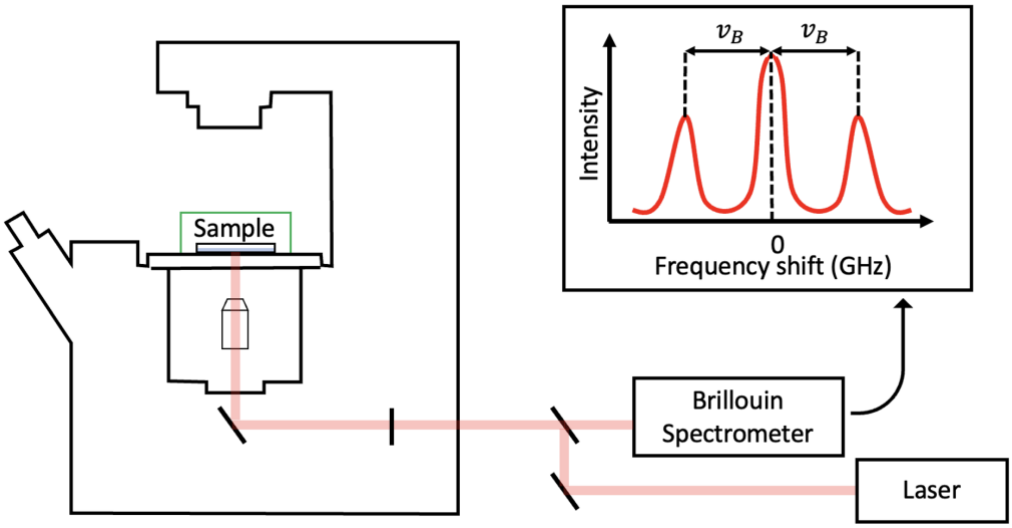

Figure 6. Schematic of an inverted confocal Brillouin setup. Laser light is sent into the sample and the backscatter is sent to the VIPA-based Brillouin spectrometer. The Brillouin spectrum is captured by an EMCCD camera. The distance of the Brillouin Stokes and anti-Stokes from the central laser peak is representative of local mechanical properties in the sample.

The illumination light and the backscattered light are distinguished by using a polarizing beam splitter and a quarter-waveplate. The collected backscatter is sent to the Brillouin spectrometer via a single mode optical fiber. This optical fiber also serves as a pinhole to ensures the backscattered light is coming from a single confocal volume. The spatial resolution of the sample is based on the objective lens used. In this dissertation, we use a 40x, 0.6 NA with a working distance: 2.7 – 4 mm.

One interesting feature of Brillouin spectroscopy come from the fact that it is not dependent on image depth, because it is not based on intensity measurements but frequency shifts measurements. For example, in fluorescence microscopy, the fluorescence intensity is heavily dependent on the imaging depth. As for Brillouin, the spectral shift is independent of the imaging depth which means the Brillouin shift is unaffected when there is intensity loss due to turbid media or samples. The main cause of signal loss is due to the low number of recovered photons in deep tissue due to Beer-Lambert law. This results in a lowered signal-to-noise ratio which lowers the instrumental precision. Previous experiments performed on large cell aggregates demonstrate the ability to measure up to 150 – 200 μm (Conrad et al., 2019).

Most VIPA-based Brillouin spectrometers for biological measurements utilize a relay telescope and a square-hole spatial filter (Scarcelli et al., 2011; Berghaus et al., 2015) sandwiched between two apodized cross-axis VIPA stages with linearly variable intensity filters (Scarcelli et al., 2015). An electron-multiplying charge-coupled device (EMCCD) camera is used to detect the diffraction pattern output by the final VIPA stage to detect the low signals. To map the sample in 3D, the microscope is fitted with a motorized stage and the laser beams raster scans the sample. The Brillouin image is acquired by recording each individual spectral for each position in the

sample. A least squares curve fit is then applied to the spectrum to determine the positions of the Brillouin peaks.

2.3. Time-lapse Brillouin measurements

An inverted confocal Brillouin microscope was used for all experiments. A single mode 660-nm continuous wave laser with power of ~30 mW was used as light source. The laser beam was focused into the sample by an objective lens (Olympus, 40×/0.6 NA) installed on an inverted microscope (Olympus, IX81), which yields a spot size of 0.7 μm × 0.7 μm × 2.6 μm. The backward scattered Brillouin signal was collected by the same objectives and analyzed by a two-stage VIPA (Light Machinery, 15 GHz FSR) based spectrometer, and the Brillouin spectrum was recorded by an EMCCD camera (Andor, iXon 897) with an exposure time of 0.05 s. Two dimensional Brillouin images were acquired by scanning the sample using a motorized stage (step size: 0.5 μm). The cross-section perpendicular to the anterior-posterior body axis was mapped by Brillouin microscope, and the averaged Brillouin shift of the neural plate region was used to represent the mechanical properties of the tissue. The Brillouin shift of the albumin is very close to that of the vitelline membrane, making it difficult to identify the boundary of neural plate tissue in the Brillouin image. To solve this issue, right before acquiring each Brillouin image, the embryo was temporarily transferred onto a different culture dish filled with Ringer's solution (Thermo Scientific, BR0052G). As soon as the Brillouin measurement is done, the embryo was transferred back to the *ex-ovo* culturing dish for continuous development. To acquire the bright-field images, a low magnification objective lens (Olympus, 4x/0.1) and a CMOS camera (Andor Neo) were used when the embryo was in the *ex-ovo* culturing dish.

2.4. Results

Fertilized white leghorn eggs were purchased from poultry farm of the University of Connecticut. For *in ovo* culturing, eggs were incubated at 37 ºC under high humidity. Incubation hours follows Hamburger-Hamilton (HH) staging (i.e. 26-29 hrs of incubation to obtain HH-4 embryo) (Hamburger and Hamilton, 1992). Time-lapse 2D mechanical imaging was performed on an inverted Brillouin microscope (Figure 7A) (see Materials and methods). By definition, Brillouin shift is positively linked to the longitudinal modulus by material properties including refractive index n and density ρ. For biological materials, the ratio of refractive index and density ρ/n^2 is found to be approximately constant (Scarcelli et al., 2013, 2015). Therefore, we here used the Brillouin shift to interpret the relative change of elastic modulus without measuring the value of the two parameters.

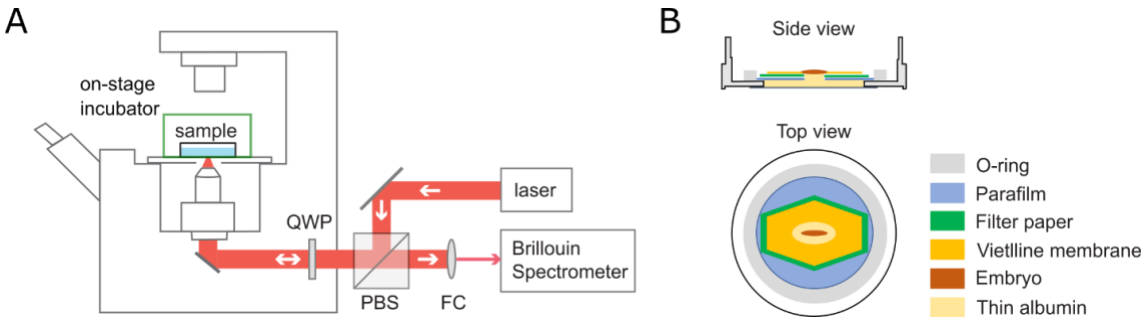

Figure 7. Schematic of the setup. (A) Confocal Brillouin microscope with on-stage incubator. QWP: quarter-wave plate; PBS: polarized beam splitter; FC: fiber coupler. (B) Carrier dish for ex-ovo culture. Side view (top) and top view (bottom) displays all components including embryo within the carrier.

The *ex-ovo* culture protocol was derived from Chapman *et al* and Schmitz *et al* (Chapman et al., 2001; Schmitz et al., 2016) with modifications for adapting to the Brillouin microscope. A 35 mm glass bottom dish with a 20 mm micro-well (Cellvis, D35-20-0-N) was used for *ex ovo* culture. A

1-inch metallic ring (Thorlabs, SM1RR) was covered with a single-layer Parafilm and a 1 cm ellipse hole was cut into the center and placed over the micro-well (inner bottom well of dish). To perform *ex ovo* culture, we used the filter paper carrier method to hold the blastoderm and vitelline membrane under tension to mimic the situation of in-ovo culturing.

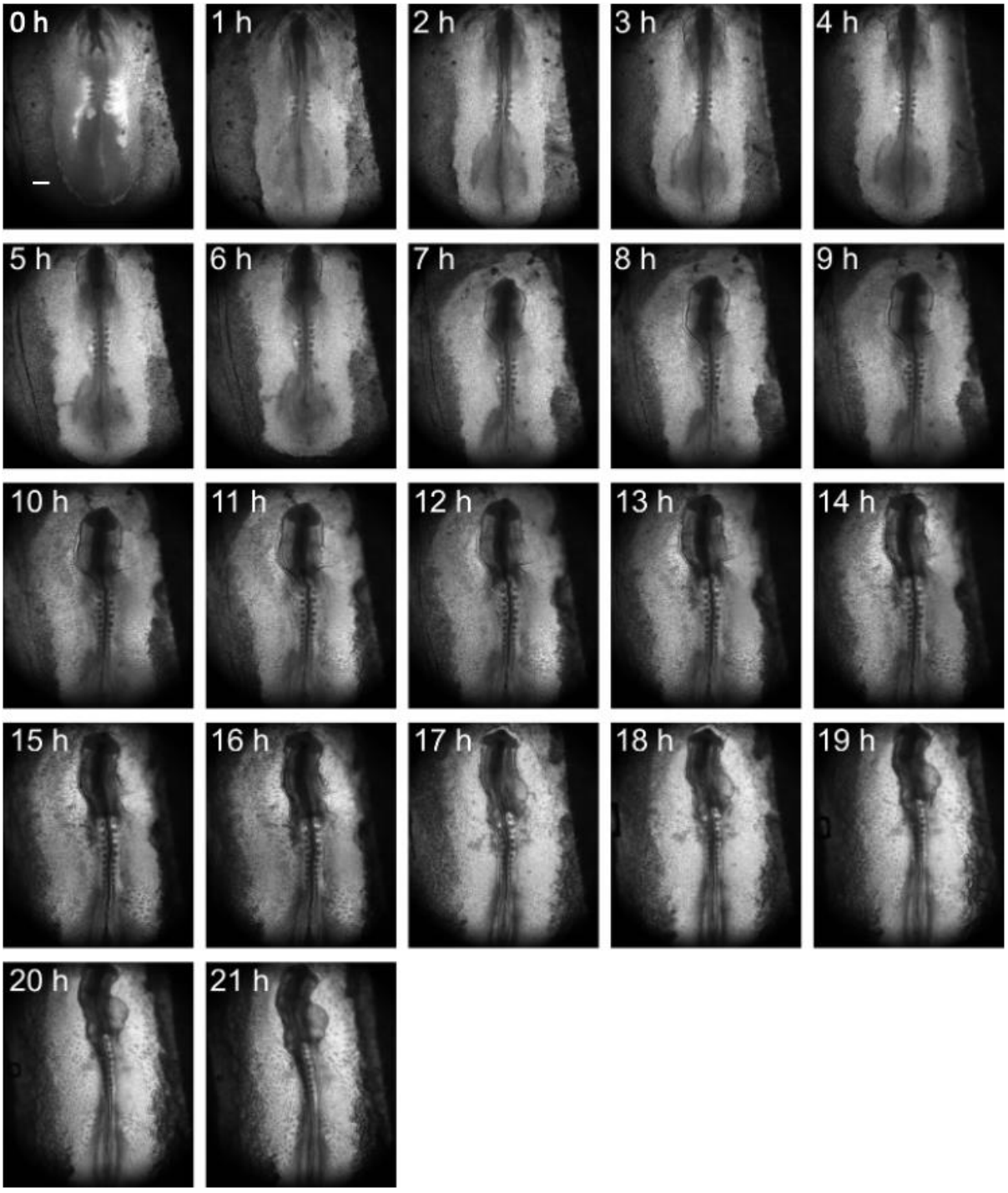

Figure 8. Brightfield time-lapse imaging of ex-ovo cultured embryo without Brillouin experiment. Representative of continuous ex-ovo development on thin albumin without any laser illumination for 21 hrs. An HH8 embryo is extracted for ex-ovo culture after 29 hrs of in-ovo incubation (0 h). Embryo is identified as HH13+ at 21 h of ex-ovo incubation (21 h) with a total incubation time of 50 hrs. Embryo develops according to the HH stages with identifiable markers at each stage. Each image taken 1 h apart. Scale bar in white representative of 300 um.

The pre-cultured embryo around HH 4 was collected from the egg and then placed dorsal side down onto a culture dish filled with thin albumin harvested from the egg (Figure 7B). Next, the dish was placed into an on-stage incubator (Warner Instruments, SA-20PLIXR-AL) for sustaining the development of the embryo (>21 hours) .

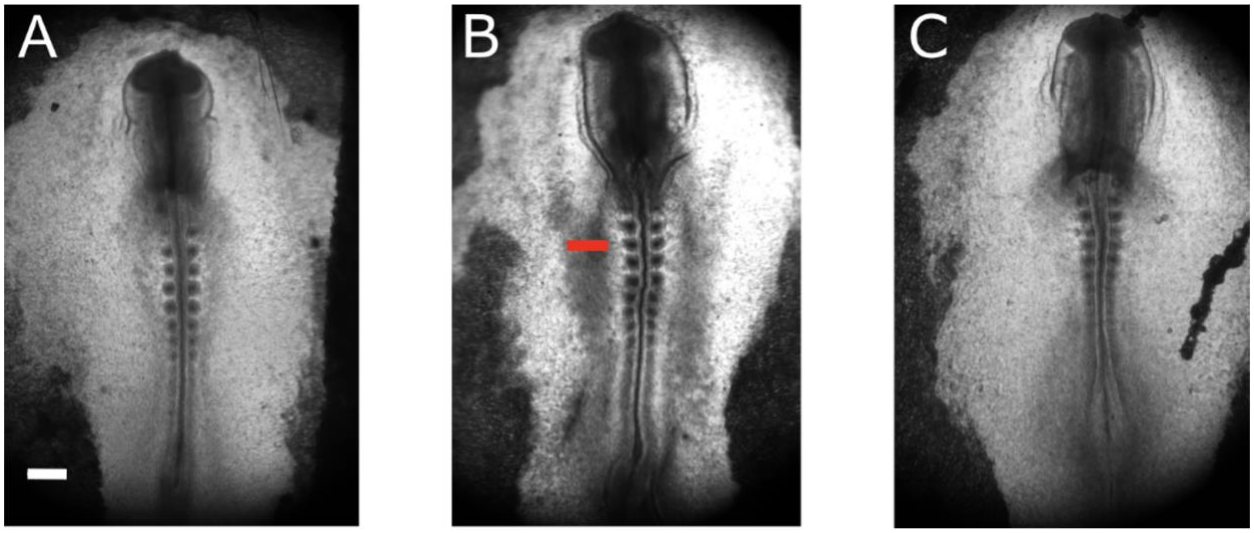

Figure 9. Comparison of all incubation and experimental methods reveal similar development. (A) HH 10 embryo after 39 hrs of continuous ex-ovo culture (30 hrs in-ovo + 9 hrs ex-ovo) on thin albumin without any laser illumination. (B) HH 10 embryo after 38 hrs of time-lapse ex-ovo culture (30 hrs in-ovo + 8 hrs ex-ovo) including transfer onto Ringer's solution and exposure to laser illumination during Brillouin acquisition. Red bar indicates location at which Brillouin

mechanical mapping was taken, at third somite position at the hindbrain/cervical boundary. (C) HH 10 embryo after 38 hrs of in-ovo culture extracted for time-point NT mapping. All three embryos experienced similar development time following HH stages and display similar morphology with different methods of incubation and experimental setting.

To ensure the ambient temperature of the embryo is about 37 ºC, the heater (Warner Instruments, TC-344C) of the on-state incubator was set to 39 +/- 0.2 ºC considering the heat dissipation from the underside of the stage which is open to the objective lens. The time-lapse bright-field images suggest the embryos from ex-ovo culture have developed with the similar time rate as those from in-ovo culture (Figure 8 and Figure 9). No morphological damage or delay in development was visibly detected.

A home-built LabView acquisition program was used to acquire both bright field images and the Brillouin spectra. For calibration of the spectrometer, Brillouin spectra of materials (water and methanol) with known Brillouin shifts were recorded and used to calculate the free spectral range and the pixel-to-frequency convention ratio. The Brillouin shift of each pixel was obtained by fit the Brillouin spectrum to a Lorentzian function. 2D Brillouin image was reconstructed from the pixel vector. Further analysis was done using MATLAB and discussed in depth in Appendices.

In-ovo cultured embryos show increased Brillouin shift of neural plate against developmental stage

To exclude any potential impact of the ex-ovo culture and the laser illumination on the tissue mechanics of neural plate, we collected in-ovo cultured embryos (N=46) at different Hamburger Hamilton (HH) stages (HH 6 to HH 12) and acquired 2D mechanical images of the cross-section perpendicular to the anterior-posterior axis using Brillouin microscope. The representative

Brillouin images suggest that the neural plate of the embryo at later stage has higher Brillouin shift than that at earlier stage (Figure 10A-10D). We then quantified the average Brillouin shift of the neural plate region for all the collected embryos. We observed that the Brillouin shift of the neural plate showed a distinct increase from HH 6 to HH 9+ and approximately maintained its value afterward (Figure 10E). The neural plate of later-stage embryo (i.e., HH 12) has an average Brillouin shift of 6.353 GHz, which is 0.126 GHz higher than that of early-stage embryos (i.e., HH 6), corresponding to ~60% increase of Young's modulus according to the empirical relationship between longitudinal modulus and Young's modulus obtained from cells (Zhang et al., 2020b).

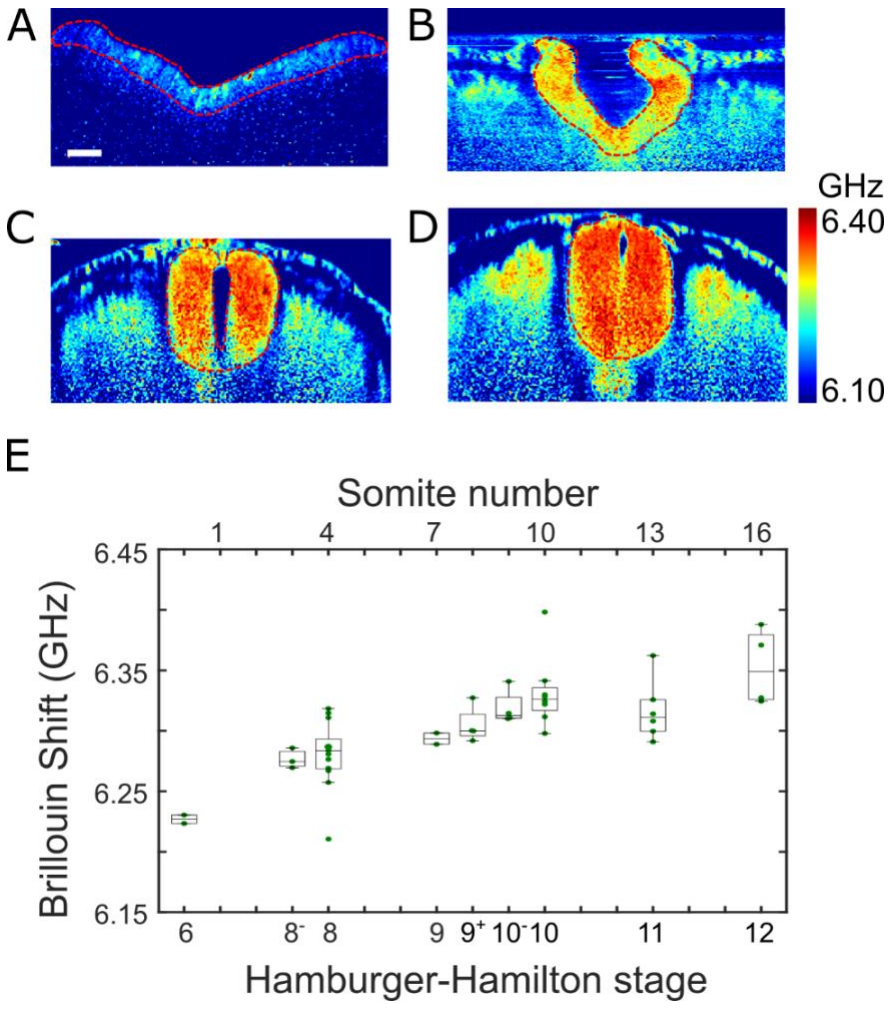

Figure 10. Result of in ovo cultured embryos. (A)-(D) Representative of four different embryos at different HH stages: (A) HH 6, (B) HH 8, (C) HH 11, (D) HH 12. Red dashed line outlines the

neural plate region. (E) Average Brillouin shifts of neural plate at different stages reveal continual tissue stiffening. Number of embryos: 46. Scalebar in white representative of 50 μm.

Time-lapse mechanical imaging of *ex-ovo* cultured embryo shows stiffening and thickening of the neural plate during NTC

To quantify the mechanical evolution of the neural plate during the entire procedure of NTC, we conducted time-lapse mechanical mapping of *ex-ovo* cultured embryo. The embryo was cultured for more than 14 hours (Figure 11), within which the time-lapse Brillouin image of the neural plate cross-section was acquired at the hindbrain/cervical region (Figure 12A).

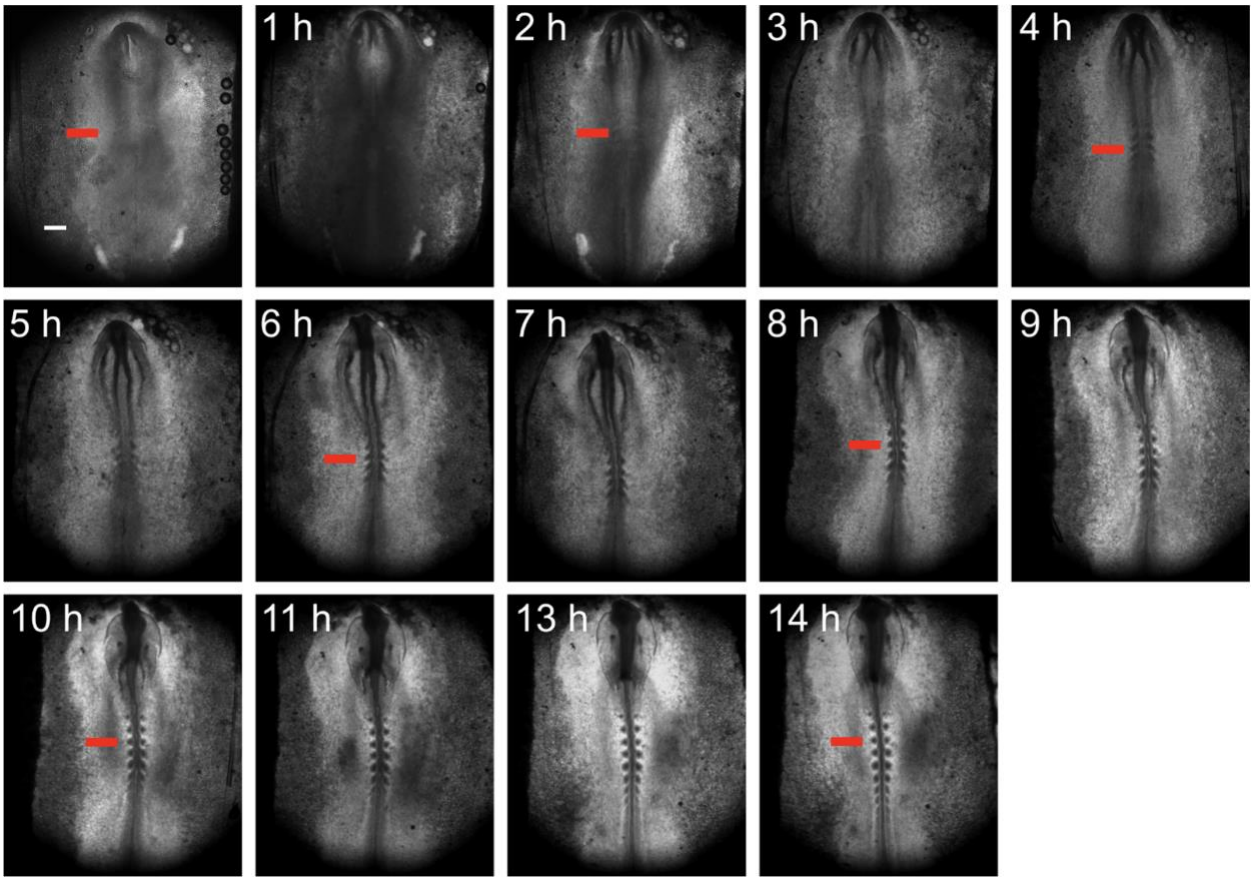

Figure 11. Brightfield time-lapse Brillouin imaging of ex-ovo cultured embryo. Representative of 14 hrs of ex-ovo development during Brillouin imaging, including transfer onto Ringer's solution

and exposure to laser illumination. An HH 8 embryo is extracted for ex-ovo culture and time-lapse Brillouin imaging after 26 hrs in-ovo incubation (0 h) and develops to an HH 10 embryo after 14 hrs of ex-ovo incubation (14 h). Brillouin acquisition occurs every 2 hrs with the initial acquisition at 0 h (HH8). This is to allow the embryo to develop on thin albumin between acquisition. Red bar indicates location at which Brillouin mechanical mapping was taken, at third somite position at the hindbrain/cervical boundary. Each image taken 1 h apart, 12 h not displayed. Scale bar in white representative of 300 um.

The result shows the average Brillouin shift of the neural plate continuously increases with culturing time (Figure 12B), which is consistent with the result of *in-ovo* cultured embryos. Repeat experiments (N=9) suggest the stiffening of the neural plate during NTC is a common phenomenon for chick embryos (Figure 12D). Specifically, the Brillouin shift of the neural plate increased significantly from HH 8- to HH 9 and remained minor change afterward. At the endpoint of *ex-ovo* culture (HH 10), the neural plates have an average Brillouin shift of 6.336 GHz, which is 0.097 GHz higher than that of the earliest stage (HH 8-), corresponding to the relative increase of ~ 46% in terms of the Young's modulus. This is consistent with the result of *in-ovo* cultured embryos, confirming that the ex-ovo culture and laser illumination did not affect the mechanical evolution of the neural plate tissue during embryonic development.

Using tissue mechanics as a contrast mechanism in Brillouin imaging, we can also quantify the morphological change of the neural plate during NTC. Here we measured the averaged thickness of the two sites that were in the middle of the distance between the median hinge point and the tips (Figure 12C). Consistent with published literatures (Colas and Schoenwolf, 2001; Lowery and Sive, 2004), we observed 4-fold thickening of the neural plate from HH 8- (~13 μm) to HH 9 (~52 μm) (Figure 12E). Intriguingly, we found that the tissue thickening and the tissue

stiffening exhibit very similar trend during the procedure of NTC. We then plotted the Brillouin shift against the thickness for all the ex-ovo cultured embryos and found a strong correlation ($p < 1 \times 10^{-6}$) between them (Figure 12F). This data suggests that the tissue stiffening and thickening are probably coordinated events for NTC.

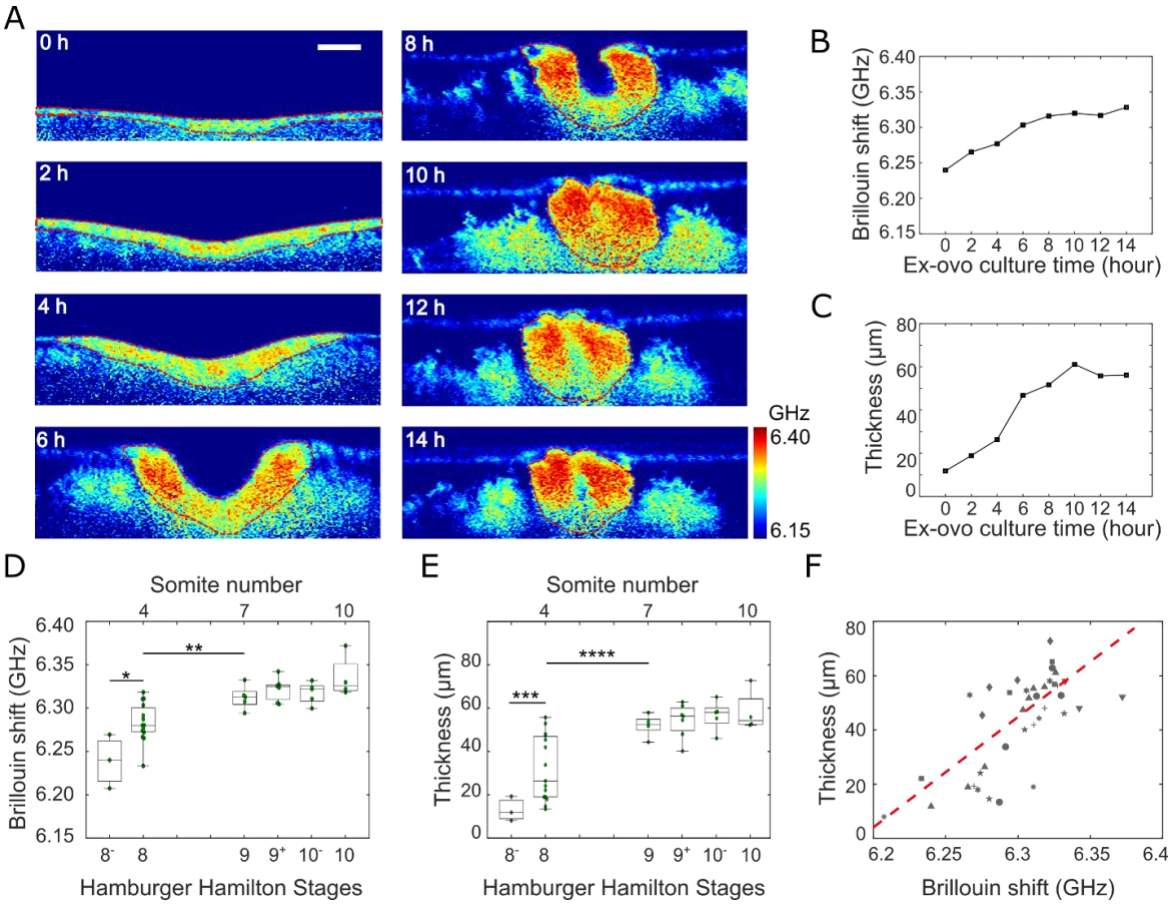

Figure 12. Time-lapse mechanical imaging of ex ovo cultured embryos. (A) Representative time-lapse Brillouin images of an embryo over 14 hours. (B) Average Brillouin shift of neural plate tissue of the embryo in (A) is increasing with culturing time. (C) Thickness of neural plate tissue of the embryo in (A) is increasing with culturing time. (D) Tissue stiffening against developmental stage is observed for all the embryos. (E) Tissue thickening against developmental stage is observed for all the embryos. (F) Correlation between average Brillouin shift and thickness of neural plate. Number of embryos: 9. Number of measurements: 39. Two-sample t test is used to

quantify the statistical significance. * p=0.008; ** p=0.012; *** p=0.049; **** p=0.01. Scalebar representative of 50 μm.

Tissue stiffening is correlated with the closure angle of neural plate during NTC

NTC is a complex biomechanical process of tissue shaping and patterning that are driven by force and mechanical properties of the tissue. Therefore, it is fundamentally necessary to understand the relationship between tissue mechanics and geometry.

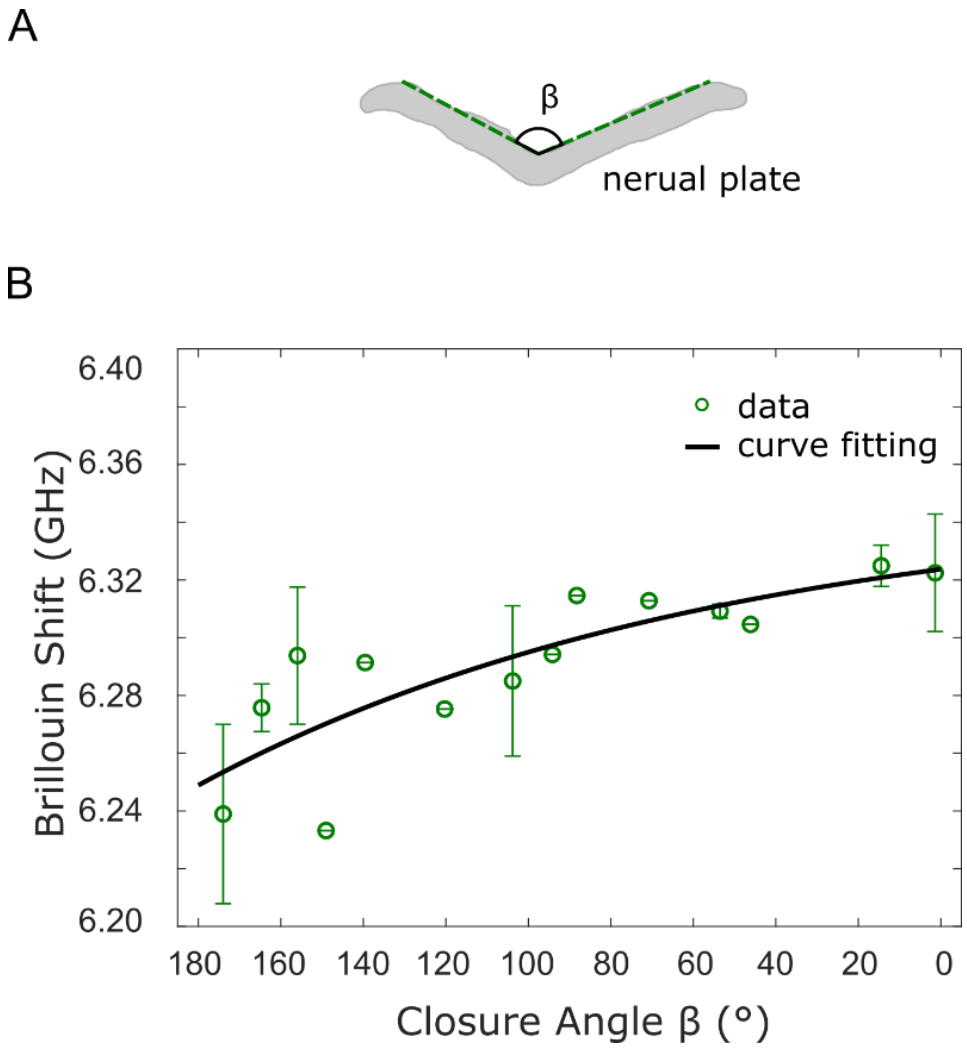

Figure 13. Tissue stiffening is correlated with tissue bending for ex-ovo cultured embryos. (A) Definition of the closure angle. (B) Closure angle is correlated with average Brillouin shift of

neural plate. Embryos are distributed into each 10° interval based on the closure angle. Data point represents the average value of the embryos within the same interval. Error bar represents the standard deviation. Solid curve is fitting result of an exponential function.

Here, we investigated how the tissue stiffening is possibly related to the geometric change of the neural plate. Based on the Brillouin images, we defined the closure angle β as the intersection of the left- and right- side neural plates at the median hinge point (Figure 13A). Next, we distributed *ex-ovo* cultured embryos into each 10º interval and calculated the averaged values for any interval having multiple embryos. We then plotted the Brillouin shift ω_B against the closure angle β (Figure 13B). The data can be well fitted by a simple exponential curve $\omega_B = A \cdot \exp(B \cdot \beta) + C$, with fitted parameters $A = -0.024, B = 7.85 \times 10^{-3}$, and $C = 6.348$. This exponential relationship suggests that the tissue stiffening is probably synchronized with the bending of the neural plate during the procedure of NTC.

3. Conclusion

The Neural Tube (NT) acts as the precursor to the central nervous system including the brain and spinal cord. Primary neurulation is the key morphogenetic event which involves the meticulous choreograph of events to manipulate the flat neural epithelium into a lumenized NT. Thus, neurulation is a complex process involving cellular, molecular and biomechanical activities (Miller and Davidson, 2013; Nikolopoulou et al., 2017). Following neural induction, convergent extension shapes the NP by simultaneously elongating and narrowing the tissue. Subsequently, the median hinge point forms, creating the neural groove, and the neural folds are elevated. Then, the dorsolateral hinge points form which appose the neural folds in preparation for fusion. Finally, the neural folds meet and fuse at the midline, completing the formation of the NT. It is well known that disruptions that occur during NTC can cause incomplete closure and result in NTD (Copp et al., 2003). While the genetic regulation and biochemical signaling of NTC have been extensively investigated, the biomechanical mechanism is less explored, and the underlying linkage between microscopic cellular/molecular activities and macroscopic morphogenesis is mostly unknown (Vijayraghavan and Davidson, 2017).

NTDs are among the commonest human birth diseases and regulated by both genetic and environmental factors (Blom et al., 2006; Copp et al., 2013). On the tissue level, NTDs arise from the physical failure of the neural tube due to the abnormal interaction of force generation and the mechanical properties of embryonic tissue. Previously, there were many different theories of the mechanisms that drove neural plate invagination (His, 1874). As experimental techniques and imaging systems improved, many theories also lost favor (Roux, 1885; Glaser, 1916; Lewis, 1947; Baker and Schroeder, 1967; Schoenwolf and Powers, 1987) and a more intrinsic mechanism (Glaser, 1916) was proposed to generate the tensions and forces necessary to drive folding. Recent

work provides strong evidence that the NTD induced by gene mutation is associated with altered tissue biomechanics (Galea et al., 2017). There also has been multiple experiments that demonstrates the prevention of NTC by applying extrinsic forces, suggesting intrinsic forces are crucial to achieve closure (van Straaten et al., 1993; Benko and Brodland, 2007). Still, little is known about how these intrinsic mechanical forces are linked to the cellular and molecular actives. In addition, it has been difficult to pinpoint the specific biomechanical processes that ensure robust neurulation. Therefore, a quantitative tool for measuring tissue mechanics should allow researchers to attribute different NTD to specific dysregulation of cellular mechanisms that cause the failure of the tissue closure, which could bridge the gap between genetic/environmental factors and tissue biomechanics and help the prevention of the diseases.

Here, we developed a new imaging modality for time-lapse mechanical mapping of live chick embryo. This modality is based on the combination of a confocal Brillouin microscope and a modified *ex-ovo* culturing system, which has subcellular resolution and enough mechanical sensitivity. Different from conventional techniques for mechanical testing, our method used a focused laser beam to quantify tissue mechanics, making it non-contact, non-invasive, and label free. We confirmed that the *ex-ovo* culture and laser illumination did not disturb the development of the embryo. We demonstrated the feasibility of this technique by acquiring 2D mechanical images of the neural plate *in situ* as the embryo was experiencing neurulation. We found that the neural plate tissue was continuously stiffened during NTC, which is consistent with previous observations (Wiebe and Brodland, 2005; Zhou et al., 2009, 2015; Barriga et al., 2018). Beyond that, we observed tissue stiffening is strongly correlated with the tissue thickening and bending.

It is worth noting that, by definition, the high-frequency longitudinal modulus measured by Brillouin scattering is different from the low-frequency or quasi-static Young's modulus

measured by conventional methods such as AFM. However, for many biological materials, it is found that the two moduli change in the same direction in response to biological activities (Scarcelli and Yun, 2018; Wu et al., 2018). Therefore, with a careful calibration for specific materials, one might utilize Brillouin data as an empirical proxy for Young's modulus. In this work, we used Brillouin shift to estimate the relative change of modulus by assuming the ratio of density and refractive index (ρ/n^2) is constant. To quantify the Brillouin modulus more accurately, Brillouin microscopy can be combined with other technique that measures the density and/or refractive index directly (Schlüßler et al., 2022). As the image depth increases, the Brillouin signal will drop depending on the transparency of the tissue. For chick embryo, the maximum penetration depth of our instrument is about 200 μm. Further improvement can be achieved by using a laser source with longer wavelength or wavefront correction techniques based on adaptive optics (Edrei and Scarcelli, 2018).

Since our time-lapse Brillouin mechanical mapping technique can directly quantify the tissue mechanics within intact live embryo, it can potentially open up new opportunities to better understand the role of biomechanical mechanism in the procedure of NTC. For example, a couple of crucial cellular activities including convergent extension (Wallingford et al., 2002), apical constriction (Sawyer et al., 2010), and interkinetic nuclear migration (Smith and Schoenwolf, 1987; Spear and Erickson, 2012) may together coordinate the observed tissue stiffening, thickening, and bending. The subcellular resolution of the Brillouin microscope will allow researchers to further investigate the role of these cellular behaviors in regulating tissue biomechanics. On the other hand, the mechanical cues can guide cell behaviors and cell fates through mechanotransduction during embryonic development (Miller and Davidson, 2013; Davis and Tapon, 2019); thus, the technique can also help understand the interaction between

biochemical signaling and biomechanics. In addition, the closure of the neural tube is physically driven by both the generated force and the mechanical resistance of the tissue (Zhou et al., 2015; Galea et al., 2017; Moon and Xiong, 2021). The *in-situ* quantification of the mechanical properties could help decouple the roles of the force and the tissue mechanics thus allow better elucidation of the biomechanical interaction. Furthermore, the computational modeling is a powerful tool to understand the mechanism of morphogenesis (Davidson et al., 2010; Nishimura et al., 2012; Murisic et al., 2015). The time-lapse mechanical images of the neural plate tissue acquired by our technique can provide new input data for the simulation of neurulation.

Appendices

A. MATLAB analysis protocol

A.1. Introduction

This section will serve to describe each step of the analysis protocol which utilizes MATLAB for each experiment.

A.2. Data collection

A homemade LabView program was created by Hongyuan Zhang and Eric Frank. LabView controls the Brillouin microscope and records the raw data coming from the VIPA-based spectrometer which is acquired with an EMCCD camera. The raw data is a series of images representative of each pixel of the imaged region. One can estimate the Brillouin shift by recording the spectra of known materials such as methanol and water at room temperature to calibrate the system. The system is calibrated with 500 repeated spectra of each material before imaging and re-acquired every hour or if laser drifting occurs. Laser drifting is clearly visible on the EMCCD image of the Brillouin spectrum. Water and methanol are prepared in glass bottles and are recorded on a calibration arm instead of the microscope body. Next, the biological sample is placed onto the microscope stage and a region of interest (ROI) may be selected. A brightfield image is recorded using the LabView program in addition to the Brillouin spectrum for each pixel of the ROI. The following files are saved in the data directory:

- `CalMeth.tdms` – data file, repeated measurements of the methanol spectrum
- `CalWater. Tdms` – data file, repeated measurements of the water spectrum
- `Brightfield.tdms` – data file, single image of the full field of view of the brightfield CMOS camera which contains the ROI

- `AcqData.tdms` – data file, acquired spectra for each pixel of the ROI

The data output by Labview are .tdms files which can be read using the function convertTDMS.m (Humphreys, 2022).

A.3. Analysis steps

Analyzing one scan

Once all the files are collected, multiple MATLAB scripts will be used to perform the remaining steps of the analysis.

Step 1. Convert all .tdms files into MATLAB readable files. Use `convert_cmos_images_from tdms.m` to convert and save the acquired brightfield images from. tdms to a readable extension/ file type such as .tiff files for lossless compression. This script will also automatically rotate the image by 90º followed by flipping horizontally to achieve the true orientation. Use `convert_tdms_calibration.m` to convert the water and methanol .tdms files into .mat files. Use `convert_tdms_userinterface_auto.m` to convert the raw camera images from .tdms files into spectra (intensity vs pixel). The spectra are then returned where each row represents pixels and each column is one recorded spectrum.

Step 2. Calculate the free spectral range (FSR) and spectral dispersion parameter PR (GHz/pixel) is calculated in `calibration_2_parameter_1.m`. Here, the user will have to load the path of the calibration files and determine the region of the EMCCD camera where the Brillouin spectrum is located. The rectangular region containing the spectrum is located. Both anti-Stokes and Stokes of the next order (Brillouin peaks) should be visible in between the left and right border of the rectangle. The user can specify the border of the rectangle to avoid stray light coming from the elastic scattering background.

For the calibration materials methanol and water, the peaks are fitted with a Lorentzian function using least squares fitting protocol in MATLAB. The separation to the center between anti-Stokes and Stokes 'sep' is calculated for water and methanol. Since the Brillouin shift of water and methanol are known, they are used to estimate the FSR and GHz/pixel ratio, PR. The Brillouin shift of methanol and water is 4.490 GHz and 6.013 GHz, respectively, with 660 nm illumination and a backscattering geometry of $\theta = 180^{o}$. First, PR is solved to convert the separate of the peaks from pixels to GHz given by:

$$PR = \frac{\omega_w - \omega_m}{sep_w^{px} - sep_m^{px}} \tag{10}$$

where the subscript denotes water (w) or methanol (m) and superscript denote the units in pixels (px). Then, the FSR is determined by the following equation:

$$FSR = g \cdot sep_m^{px} + 2 \cdot \omega_m \tag{11}$$

Then, the peak separation in GHz can be determined by the following:

$$sep_m^{GHz} = FSR - 2 \cdot \omega_m \tag{12}$$

$$sep_w^{GHz} = FSR - 2 \cdot \omega_w \tag{13}$$

Step 3. Using the PR and FSR, we are now able to start the fitting of the experimental data. Using `cal.m`, the path for the directory of the acquired spectra (AcqData.tdms) is mapped and user can manually change the name and re-run the script section for each imaged ROI. Analyzing the scanned ROI is the rate limiting step in the analysis process.

Step 4. Each spectrum is fitted with a Lorentzian function and the distance between the peak centers is calculated and recorded as the variable sep. Then, the Brillouin shift for each pixel in the ROI is calculated with the following:

$$\omega_B = \frac{FSR - sep \cdot PR}{2} \quad (14)$$

The Brillouin linewidth is calculated by taking the average of the full width half maximum of each fitted peak multiplied by the PR value. The Brillouin intensity is calculated as the average intensity of the two fitted peaks. These images are useful for identifying areas of an ROI that may have low signal due to scattering. Low signal may also present itself in the form of precision loss in the Brillouin shift image but will be more evident in the Brillouin linewidth image.

Step 5. In `embryo_analysis.m`, a .mat file containing all the Brillouin shift for each pixel of the capture image is recorded in `BiM1.mat`. The Brillouin image can be reconstructed by inputting the step size of the x-range of the ROI. Using `roipoly` from the Image Processing Toolbox, a mask is created over a ROI to be further analyzed can be selected. `roipoly` returns a binary image.

Step 6. Finally, Obtain the averaged Brillouin shift for the ROI selected in step 5 by multiplying the Brillouin shift recorded in `BiM1.mat` with the mask created using `roipoly.` The averaged Brillouin shift is then taken from masked region. All of the variables created can be saved in the directory allowing the user to quickly load the fitting result, re-display the image, or repeat any step of the analysis in MATLAB by reopening any previous .m files.

A.4. Conclusion

This appendix describes the steps necessary to analyze experimental Brillouin imaging data. The mechanical properties of the NT are highly variable parameters. Thus, efficient data processing and organization is imperative for investigating the mechanical events that occur during neurulation.

Bibliography

Baker, P.C., Schroeder, T.E., 1967. Cytoplasmic filaments and morphogenetic movement in the amphibian neural tube. Dev. Biol. 15, 432–450. https://doi.org/10.1016/0012-1606(67)90036-X

Barriga, E.H., Franze, K., Charras, G., Mayor, R., 2018. Tissue stiffening coordinates morphogenesis by triggering collective cell migration in vivo. Nature 554, 523–527. https://doi.org/10.1038/nature25742

Beloussov, L.V., Dorfman, J.G., Cherdantzev, V.G., 1975. Mechanical stresses and morphological patterns in amphibian embryos. J. Embryol. Exp. Morphol. 34, 559–574.

Benko, R., Brodland, G.W., 2007. Measurement of in vivo Stress Resultants in Neurulation-stage Amphibian Embryos. Ann. Biomed. Eng. 35, 672–681. https://doi.org/10.1007/s10439-006-9250-1

Berghaus, K., Zhang, J., Yun, S.H., Scarcelli, G., 2015. High-finesse sub-GHz-resolution spectrometer employing VIPA etalons of different dispersion. Opt. Lett. 40, 4436. https://doi.org/10.1364/OL.40.004436

Blom, H.J., Shaw, G.M., den Heijer, M., Finnell, R.H., 2006. Neural tube defects and folate: case far from closed. Nat. Rev. Neurosci. 7, 724–731. https://doi.org/10.1038/nrn1986

Boyd, R.W., 2003. Nonlinear Optics - 3rd Edition, 3rd ed. Academic Press.

Brillouin, L., 1922. Diffusion de la lumière et des rayons X par un corps transparent homogène - Influence de l'agitation thermique. Ann. Phys. 9, 88–122. https://doi.org/10.1051/anphys/192209170088

Brun, R.B., Garson, J.A., 1983. Neurulation in the Mexican salamander {Ambystoma mexicanum): a drug study and cell shape analysis of the epidermis and the neural plate. J. Embryol. Exp. Morphol. 74, 22.

Campàs, O., Mammoto, T., Hasso, S., Sperling, R.A., O'Connell, D., Bischof, A.G., Maas, R., Weitz, D.A., Mahadevan, L., Ingber, D.E., 2014. Quantifying cell-generated mechanical forces within living embryonic tissues. Nat. Methods 11, 183–189. https://doi.org/10.1038/nmeth.2761

Chevalier, N.R., Gazquez, E., Dufour, S., Fleury, V., 2016. Measuring the micromechanical properties of embryonic tissues. Methods San Diego Calif 94, 120–128. https://doi.org/10.1016/j.ymeth.2015.08.001

Chhetri, P.K., Das, J.M., 2021. [Figure, neural crest cells. Contributed by...] [WWW Document]. URL https://www.ncbi.nlm.nih.gov/books/NBK557414/figure/article-74451.image.f2/ (accessed 8.2.22).

Colas, J.F., Schoenwolf, G.C., 2001. Towards a cellular and molecular understanding of neurulation. Dev. Dyn. Off. Publ. Am. Assoc. Anat. 221, 117–145. https://doi.org/10.1002/dvdy.1144

Conrad, C., Gray, K.M., Stroka, K.M., Rizvi, I., Scarcelli, G., 2019. Mechanical Characterization of 3D Ovarian Cancer Nodules Using Brillouin Confocal Microscopy. Cell. Mol. Bioeng. 12, 215–226. https://doi.org/10.1007/s12195-019-00570-7

Copp, A.J., Adzick, N.S., Chitty, L.S., Fletcher, J.M., Holmbeck, G.N., Shaw, G.M., 2015. Spina Bifida. Nat. Rev. Dis. Primer 1, 15007. https://doi.org/10.1038/nrdp.2015.7

Copp, A.J., Greene, N.D.E., Murdoch, J.N., 2003. The genetic basis of mammalian neurulation. Nat. Rev. Genet. 4, 784–793. https://doi.org/10.1038/nrg1181
Copp, A.J., Stanier, P., Greene, N.D.E., 2013. Neural tube defects: recent advances, unsolved questions, and controversies. Lancet Neurol. 12, 799–810. https://doi.org/10.1016/S1474-4422(13)70110-8
Davidson, L.A., 2012. Epithelial machines that shape the embryo. Trends Cell Biol. 22, 82–87. https://doi.org/10.1016/j.tcb.2011.10.005
Davidson, L.A., Joshi, S.D., Kim, H.Y., von Dassow, M., Zhang, L., Zhou, J., 2010. Emergent morphogenesis: elastic mechanics of a self-deforming tissue. J. Biomech. 43, 63. https://doi.org/10.1016/j.jbiomech.2009.09.010
Davidson, L.A., Keller, R.E., 1999. Neural tube closure in Xenopus laevis involves medial migration, directed protrusive activity, cell intercalation and convergent extension. Development 126, 10.
Davidson, L.A., Koehl, M.A.R., Keller, R., Oster, G.F., 1995. How do sea urchins invaginate? Using biomechanics to distinguish between mechanisms of primary invagination. Dev. Camb. Engl. 121, 14.
Davidson, L.A., Marsden, M., Keller, R., DeSimone, D.W., 2006. Integrin α5β1 and Fibronectin Regulate Polarized Cell Protrusions Required for Xenopus Convergence and Extension. Curr. Biol. 16, 833–844. https://doi.org/10.1016/j.cub.2006.03.038
Davis, J.R., Tapon, N., 2019. Hippo signalling during development. Dev. Camb. Engl. 146, dev167106. https://doi.org/10.1242/dev.167106
Dil, J.G., 1982. Brillouin scattering in condensed matter. Rep. Prog. Phys. 45, 285–334. https://doi.org/10.1088/0034-4885/45/3/002
Duck, F.A., 1990. Physical Properties of Tissues: A Comprehensive Reference Book. Academic Press.
Edrei, E., Gather, M.C., Scarcelli, G., 2017. Integration of spectral coronagraphy within VIPA-based spectrometers for high extinction Brillouin imaging. Opt. Express 25, 6895–6903. https://doi.org/10.1364/OE.25.006895
Edrei, E., Scarcelli, G., 2018. Brillouin micro-spectroscopy through aberrations via sensorless adaptive optics. Appl. Phys. Lett. 112, 163701. https://doi.org/10.1063/1.5027838
Fabry, B., Maksym, G.N., Butler, J.P., Glogauer, M., Navajas, D., Fredberg, J.J., 2001. Scaling the Microrheology of Living Cells. Phys. Rev. Lett. 87, 148102. https://doi.org/10.1103/PhysRevLett.87.148102
Fabry, C., Perot, A., 1897. Sur les franges des lames minces argent ees et leur application a la mesure de petites epaisseurs d'air. Ann. Chim. Phys. 12.
Fiore, A., 2021. Brillouin Confocal Microscopy in Off-Axis Configuration (Ph.D.). University of Maryland, College Park, United States -- Maryland.
Fiore, A., Zhang, J., Shao, P., Yun, S.H., Scarcelli, G., 2016. High-extinction virtually imaged phased array-based Brillouin spectroscopy of turbid biological media. Appl. Phys. Lett. 108, 203701. https://doi.org/10.1063/1.4948353
Franze, K., 2011. Atomic force microscopy and its contribution to understanding the development of the nervous system. Curr. Opin. Genet. Dev. 21, 530–537. https://doi.org/10.1016/j.gde.2011.07.001

Galea, G.L., Cho, Y.-J., Galea, G., Molè, M.A., Rolo, A., Savery, D., Moulding, D., Culshaw, L.H., Nikolopoulou, E., Greene, N.D.E., Copp, A.J., 2017. Biomechanical coupling facilitates spinal neural tube closure in mouse embryos. Proc. Natl. Acad. Sci. 114, E5177–E5186. https://doi.org/10.1073/pnas.1700934114

Glaser, O.C., 1916. The Theory of Autonomous Folding in Embryogenesis. Science 44, 505–509.

Hamburger, V., Hamilton, H.L., 1992. A series of normal stages in the development of the chick embryo. 1951. Dev. Dyn. Off. Publ. Am. Assoc. Anat. 195, 231–272. https://doi.org/10.1002/aja.1001950404

Heer, N.C., Martin, A.C., 2017. Tension, contraction and tissue morphogenesis. Dev. Camb. Engl. 144, 4249–4260. https://doi.org/10.1242/dev.151282

His, W., 1874. Unsere Koerperform und das physiologische Problem ihrer Entstehung: Briefe an einen befreundeten Naturforscher. F.C.W. Vogel.

Hoff, K. vS., Wassersug, R.J., 2000. Tadpole Locomotion: Axial Movement and Tail Functions in a Largely Vertebraeless Vertebrate1. Am. Zool. 40, 62–076. https://doi.org/10.1093/icb/40.1.62

Humphrey, J.D., 2001. Stress, Strain, and Mechanotransduction in Cells. J. Biomech. Eng. 123, 638–641. https://doi.org/10.1115/1.1406131

Humphreys, B., 2022. ConvertTDMS.

Karfunkel, P., 1972. The activity of microtubules and microfilaments in neurulation in the chick. J. Exp. Zool. 181, 289–301. https://doi.org/10.1002/jez.1401810302

Karfunkel, P., 1971. The role of microtubules and microfilaments in neurulation in Xenopus. Dev. Biol. 25, 30–56. https://doi.org/10.1016/0012-1606(71)90018-2

Kim, K., Guck, J., 2020. The Relative Densities of Cytoplasm and Nuclear Compartments Are Robust against Strong Perturbation. Biophys. J. 119, 1946–1957. https://doi.org/10.1016/j.bpj.2020.08.044

Kitchin, I.C., 1949. The effects of notochordectomy in Amblystoma mexicanum. J. Exp. Zool. 112, 393–415. https://doi.org/10.1002/jez.1401120303

Koehl, M.A.R., 1990. Biomechanical approaches to morphogenesis. Semin. Dev. Biol. 1, 367–378.

Kofron, M., Heasman, J., Lang, S.A., Wylie, C.C., 2002. Plakoglobin is required for maintenance of the cortical actin skeleton in early Xenopus embryos and for cdc42-mediated wound healing. J. Cell Biol. 158, 695–708. https://doi.org/10.1083/jcb.200202123

Lee, G., Hynes, R., Kirschner, M., 1984. Temporal and spatial regulation of fibronectin in early Xenopus development. Cell 36, 729–740. https://doi.org/10.1016/0092-8674(84)90353-2

Lee, S.A., Lindsay, S.M., Powell, J.W., Weidlich, T., Tao, N.J., Lewen, G.D., Rupprecht, A., 1987. A Brillouin scattering study of the hydration of Li- and Na-DNA films. Biopolymers 26, 1637–1665. https://doi.org/10.1002/bip.360261002

Lees, S., Tao, N.-J., Lindsay, S.M., 1990. Studies of Compact Hard Tissues and Collagen by Means of Brillouin Light Scattering. Connect. Tissue Res. 24, 187–205. https://doi.org/10.3109/03008209009152148

Levental, I., Georges, P.C., Janmey, P.A., 2007. Soft biological materials and their impact on cell function. Soft Matter 3, 299–306. https://doi.org/10.1039/B610522J

Lewis, W.H., 1947. Mechanics of invagination. Anat. Rec. 97, 139–156. https://doi.org/10.1002/ar.1090970203

Lozano, R., Naghavi, M., Foreman, K., Lim, S., Shibuya, K., Aboyans, V., Abraham, J., Adair, T., Aggarwal, R., Ahn, S.Y., AlMazroa, M.A., Alvarado, M., Anderson, H.R., Anderson, L.M., Andrews, K.G., Atkinson, C., Baddour, L.M., Barker-Collo, S., Bartels, D.H., Bell, M.L., Benjamin, E.J., Bennett, D., Bhalla, K., Bikbov, B., Abdulhak, A.B., Birbeck, G., Blyth, F., Bolliger, I., Boufous, S., Bucello, C., Burch, M., Burney, P., Carapetis, J., Chen, H., Chou, D., Chugh, S.S., Coffeng, L.E., Colan, S.D., Colquhoun, S., Colson, K.E., Condon, J., Connor, M.D., Cooper, L.T., Corriere, M., Cortinovis, M., de Vaccaro, K.C., Couser, W., Cowie, B.C., Criqui, M.H., Cross, M., Dabhadkar, K.C., Dahodwala, N., De Leo, D., Degenhardt, L., Delossantos, A., Denenberg, J., Des Jarlais, D.C., Dharmaratne, S.D., Dorsey, E.R., Driscoll, T., Duber, H., Ebel, B., Erwin, P.J., Espindola, P., Ezzati, M., Feigin, V., Flaxman, A.D., Forouzanfar, M.H., Fowkes, F.G.R., Franklin, R., Fransen, M., Freeman, M.K., Gabriel, S.E., Gakidou, E., Gaspari, F., Gillum, R.F., Gonzalez-Medina, D., Halasa, Y.A., Haring, D., Harrison, J.E., Havmoeller, R., Hay, R.J., Hoen, B., Hotez, P.J., Hoy, D., Jacobsen, K.H., James, S.L., Jasrasaria, R., Jayaraman, S., Johns, N., Karthikeyan, G., Kassebaum, N., Keren, A., Khoo, J.-P., Knowlton, L.M., Kobusingye, O., Koranteng, A., Krishnamurthi, R., Lipnick, M., Lipshultz, S.E., Ohno, S.L., Mabweijano, J., MacIntyre, M.F., Mallinger, L., March, L., Marks, G.B., Marks, R., Matsumori, A., Matzopoulos, R., Mayosi, B.M., McAnulty, J.H., McDermott, M.M., McGrath, J., Memish, Z.A., Mensah, G.A., Merriman, T.R., Michaud, C., Miller, M., Miller, T.R., Mock, C., Mocumbi, A.O., Mokdad, A.A., Moran, A., Mulholland, K., Nair, M.N., Naldi, L., Narayan, K.M.V., Nasseri, K., Norman, P., O'Donnell, M., Omer, S.B., Ortblad, K., Osborne, R., Ozgediz, D., Pahari, B., Pandian, J.D., Rivero, A.P., Padilla, R.P., Perez-Ruiz, F., Perico, N., Phillips, D., Pierce, K., Pope, C.A., Porrini, E., Pourmalek, F., Raju, M., Ranganathan, D., Rehm, J.T., Rein, D.B., Remuzzi, G., Rivara, F.P., Roberts, T., De León, F.R., Rosenfeld, L.C., Rushton, L., Sacco, R.L., Salomon, J.A., Sampson, U., Sanman, E., Schwebel, D.C., Segui-Gomez, M., Shepard, D.S., Singh, D., Singleton, J., Sliwa, K., Smith, E., Steer, A., Taylor, J.A., Thomas, B., Tleyjeh, I.M., Towbin, J.A., Truelsen, T., Undurraga, E.A., Venketasubramanian, N., Vijayakumar, L., Vos, T., Wagner, G.R., Wang, M., Wang, W., Watt, K., Weinstock, M.A., Weintraub, R., Wilkinson, J.D., Woolf, A.D., Wulf, S., Yeh, P.-H., Yip, P., Zabetian, A., Zheng, Z.-J., Lopez, A.D., Murray, C.J., 2012. Global and regional mortality from 235 causes of death for 20 age groups in 1990 and 2010: a systematic analysis for the Global Burden of Disease Study 2010. The Lancet 380, 2095–2128. https://doi.org/10.1016/S0140-6736(12)61728-0

Mai, C.T., Cassell, C.H., Meyer, R.E., Isenburg, J., Canfield, M.A., Rickard, R., Olney, R.S., Stallings, E.B., Beck, M., Hashmi, S.S., Cho, S.J., Kirby, R.S., for the National Birth Defects Prevention Network, 2014. Birth defects data from population-based birth defects surveillance programs in the United States, 2007 to 2011: Highlighting orofacial clefts: Orofacial Clefts Birth Defects Data. Birt. Defects Res. A. Clin. Mol. Teratol. 100, 895–904. https://doi.org/10.1002/bdra.23329

Marrese, M., Antonovaite, N., Nelemans, B.K.A., Smit, T.H., Iannuzzi, D., 2019. Micro-indentation and optical coherence tomography for the mechanical characterization of

embryos: Experimental setup and measurements on chicken embryos. Acta Biomater. 97, 524–534. https://doi.org/10.1016/j.actbio.2019.07.056
Mielke, A.F., Elam, K.A., 2009. Dynamic measurement of temperature, velocity, and density in hot jets using Rayleigh scattering. Exp. Fluids 47, 673–688. https://doi.org/10.1007/s00348-009-0708-4
Miller, C.J., Davidson, L., 2013. The interplay between cell signaling and mechanics in developmental processes. Nat. Rev. Genet. 14, 733–744. https://doi.org/10.1038/nrg3513
Moon, L.D., Xiong, F., 2021. Mechanics of neural tube morphogenesis. Semin. Cell Dev. Biol. https://doi.org/10.1016/j.semcdb.2021.09.009
Morita, H., Kajiura-Kobayashi, H., Takagi, C., Yamamoto, T.S., Nonaka, S., Ueno, N., 2012. Cell movements of the deep layer of non-neural ectoderm underlie complete neural tube closure in *Xenopus*. Development 139, 1417–1426. https://doi.org/10.1242/dev.073239
Morris, J., Rankin, J., Draper, E., Kurinczuk, J., Springett, A., Tucker, D., Wellesley, D., Wreyford, B., Wald, N., 2016. Prevention of neural tube defects in the UK: a missed opportunity. Arch. Dis. Child. 101, 604–607. https://doi.org/10.1136/archdischild-2015-309226
Murisic, N., Hakim, V., Kevrekidis, I.G., Shvartsman, S.Y., Audoly, B., 2015. From Discrete to Continuum Models of Three-Dimensional Deformations in Epithelial Sheets. Biophys. J. 109, 154–163. https://doi.org/10.1016/j.bpj.2015.05.019
Nikolić, M., 2022. HIGH RESOLUTION MAPPING OF INTRACELLULAR MECHANICAL PROPERTIES DURING KEY STAGES OF CANCER PROGRESSION (Ph.D.). University of Maryland, College Park, United States -- Maryland.
Nikolopoulou, E., Galea, G.L., Rolo, A., Greene, N.D.E., Copp, A.J., 2017. Neural tube closure: cellular, molecular and biomechanical mechanisms. Dev. Camb. Engl. 144, 552–566. https://doi.org/10.1242/dev.145904
Nishimura, T., Honda, H., Takeichi, M., 2012. Planar cell polarity links axes of spatial dynamics in neural-tube closure. Cell 149, 1084–1097. https://doi.org/10.1016/j.cell.2012.04.021
Prevedel, R., Diz-Muñoz, A., Ruocco, G., Antonacci, G., 2019. Brillouin microscopy: an emerging tool for mechanobiology. Nat. Methods 16, 969–977. https://doi.org/10.1038/s41592-019-0543-3
Raghunathan, R., Zhang, J., Wu, C., Rippy, J., Singh, M., Larin, K.V., Scarcelli, G., 2017. Evaluating biomechanical properties of murine embryos using Brillouin microscopy and optical coherence tomography. J. Biomed. Opt. 22, 086013. https://doi.org/10.1117/1.JBO.22.8.086013
Randall, J., Vaughan, J.M., Cusak, S., 1979. Brillouin Scattering in Systems of Biological Significance [and Discussion]. Philos. Trans. R. Soc. Lond. Ser. Math. Phys. Sci. 293, 341–348.
Ray, H.J., Niswander, L., 2012. Mechanisms of tissue fusion during development. Development 139, 1701–1711. https://doi.org/10.1242/dev.068338
Roux, W., 1885. Beitrage zur Morphologie der funktionellen Anpassung. Arch Anat Physiol Anat Abt 120–185.
Savin, T., Kurpios, N.A., Shyer, A.E., Florescu, P., Liang, H., Mahadevan, L., Tabin, C.J., 2011. On the growth and form of the gut. Nature 476, 57–62. https://doi.org/10.1038/nature10277

Sawyer, J.M., Harrell, J.R., Shemer, G., Sullivan-Brown, J., Roh-Johnson, M., Goldstein, B., 2010. Apical constriction: a cell shape change that can drive morphogenesis. Dev. Biol. 341, 5–19. https://doi.org/10.1016/j.ydbio.2009.09.009

Scarcelli, G., Kim, P., Yun, S.H., 2011. In Vivo Measurement of Age-Related Stiffening in the Crystalline Lens by Brillouin Optical Microscopy. Biophys. J. 101, 1539–1545. https://doi.org/10.1016/j.bpj.2011.08.008

Scarcelli, G., Kim, P., Yun, S.H., 2008. Cross-axis cascading of spectral dispersion. Opt. Lett. 33, 2979. https://doi.org/10.1364/OL.33.002979

Scarcelli, G., Kling, S., Quijano, E., Pineda, R., Marcos, S., Yun, S.H., 2013. Brillouin Microscopy of Collagen Crosslinking: Noncontact Depth-Dependent Analysis of Corneal Elastic Modulus. Invest. Ophthalmol. Vis. Sci. 54, 1418–1425. https://doi.org/10.1167/iovs.12-11387

Scarcelli, G., Pineda, R., Yun, S.H., 2012. Brillouin Optical Microscopy for Corneal Biomechanics. Invest. Ophthalmol. Vis. Sci. 53, 185–190. https://doi.org/10.1167/iovs.11-8281

Scarcelli, G., Polacheck, W.J., Nia, H.T., Patel, K., Grodzinsky, A.J., Kamm, R.D., Yun, S.H., 2015. Noncontact three-dimensional mapping of intracellular hydromechanical properties by Brillouin microscopy. Nat. Methods 12, 1132–1134. https://doi.org/10.1038/nmeth.3616

Scarcelli, G., Yun, S.H., 2018. Reply to 'Water content, not stiffness, dominates Brillouin spectroscopy measurements in hydrated materials.' Nat. Methods 15, 562–563. https://doi.org/10.1038/s41592-018-0075-2

Scarcelli, G., Yun, S.H., 2008. Confocal Brillouin microscopy for three-dimensional mechanical imaging. Nat. Photonics 2, 39–43. https://doi.org/10.1038/nphoton.2007.250

Schlüßler, R., Kim, K., Nötzel, M., Taubenberger, A., Abuhattum, S., Beck, T., Müller, P., Maharana, S., Cojoc, G., Girardo, S., Hermann, A., Alberti, S., Guck, J., 2022. Correlative all-optical quantification of mass density and mechanics of subcellular compartments with fluorescence specificity. eLife 11, e68490. https://doi.org/10.7554/eLife.68490

Schoenwolf, G.C., Powers, M.L., 1987. Shaping of the chick neuroepithelium during primary and secondary neurulation: Role of cell elongation. Anat. Rec. 218, 182–195. https://doi.org/10.1002/ar.1092180214

Schoenwolf, G.C., Smith, J.L., 1990. Mechanisms of neurulation: traditional viewpoint and recent advances. Development 109, 243–270. https://doi.org/10.1242/dev.109.2.243

Schroeder, T.E., 1970. Neurulation in Xenopus laevis. An analysis and model based upon light and electron microscopy | Development | The Company of Biologists. Development 23, 427–462.

Skoglund, P., Dzamba, B., Coffman, C. r., Harris, W. a., Keller, R., 2006. Xenopus fibrillin is expressed in the organizer and is the earliest component of matrix at the developing notochord-somite boundary. Dev. Dyn. 235, 1974–1983. https://doi.org/10.1002/dvdy.20818

Smith, J.L., Schoenwolf, G.C., 1987. Cell cycle and neuroepithelial cell shape during bending of the chick neural plate. Anat. Rec. 218, 196–206. https://doi.org/10.1002/ar.1092180215

Spear, P.C., Erickson, C.A., 2012. Interkinetic nuclear migration: A mysterious process in search of a function. Dev. Growth Differ. 54, 306–316. https://doi.org/10.1111/j.1440-169X.2012.01342.x

Talbot, W.S., Trevarrow, B., Halpern, M.E., Melby, A.E., Farr, G., Postlethwait, J.H., Jowett, T., Kimmel, C.B., Kimelman, D., 1995. A homeobox gene essential for zebrafish notochord development. Nature 378, 150–157. https://doi.org/10.1038/378150a0

Tao, Q., Nandadasa, S., McCrea, P.D., Heasman, J., Wylie, C., 2007. G-protein-coupled signals control cortical actin assembly by controlling cadherin expression in the early Xenopus embryo. Development 134, 2651–2661. https://doi.org/10.1242/dev.002824

van Straaten, H.W., Hekking, J.W., Consten, C., Copp, A.J., 1993. Intrinsic and extrinsic factors in the mechanism of neurulation: effect of curvature of the body axis on closure of the posterior neuropore. Development 117, 1163–1172. https://doi.org/10.1242/dev.117.3.1163

Van Straaten, H.W.M., Janssen, H.C.J.P., Peeters, M.C.E., Copp, A.J., Hekking, J.W.M., 1996. Neural tube closure in the chick embryo is multiphasic. Dev. Dyn. 207, 309–318. https://doi.org/10.1002/(SICI)1097-0177(199611)207:3<309::AID-AJA8>3.0.CO;2-L

Vijayraghavan, D.S., Davidson, L.A., 2017. Mechanics of neurulation: From classical to current perspectives on the physical mechanics that shape, fold, and form the neural tube. Birth Defects Res. 109, 153–168. https://doi.org/10.1002/bdra.23557

Wallingford, J.B., Fraser, S.E., Harland, R.M., 2002. Convergent Extension: The Molecular Control of Polarized Cell Movement during Embryonic Development. Dev. Cell 2, 695–706. https://doi.org/10.1016/S1534-5807(02)00197-1

Wallingford, J.B., Niswander, L.A., Shaw, G.M., Finnell, R.H., 2013. The Continuing Challenge of Understanding, Preventing, and Treating Neural Tube Defects. Science 339, 1222002. https://doi.org/10.1126/science.1222002

Wassersug, R.J., 1989. Locomotion in Amphibian Larvae (or "Why Aren't Tadpoles Built Like Fishes?"). Am. Zool. 29, 65–84. https://doi.org/10.1093/icb/29.1.65

Waters, C.M., Sporn, P.H.S., Liu, M., Fredberg, J.J., 2002. Cellular biomechanics in the lung. Am. J. Physiol.-Lung Cell. Mol. Physiol. 283, L503–L509. https://doi.org/10.1152/ajplung.00141.2002

Wedlich, D., Klein, G., Hacke, H., 1989. The distribution of fibronectin and laminin in the somitogenesis of Xenopus laevis. Differentiation 40, 77–83. https://doi.org/10.1111/j.1432-0436.1989.tb00816.x

Welte, M.A., Gross, S.P., Postner, M., Block, S.M., Wieschaus, E.F., 1998. Developmental Regulation of Vesicle Transport in Drosophila Embryos: Forces and Kinetics. Cell 92, 547–557. https://doi.org/10.1016/S0092-8674(00)80947-2

Wen, J., Liu, J., Lau, K., Liu, H., Hopyan, S., Sun, Y., 2015. Automated micro-aspiration of mouse embryo limb bud tissue, in: 2015 IEEE International Conference on Robotics and Automation (ICRA). Presented at the 2015 IEEE International Conference on Robotics and Automation (ICRA), pp. 2667–2672. https://doi.org/10.1109/ICRA.2015.7139559

Wiebe, C., Brodland, G.W., 2005. Tensile properties of embryonic epithelia measured using a novel instrument. J. Biomech. 38, 2087–2094. https://doi.org/10.1016/j.jbiomech.2004.09.005

Wilde, J.J., Petersen, J.R., Niswander, L., 2014. Genetic, Epigenetic, and Environmental Contributions to Neural Tube Closure. Annu. Rev. Genet. 48, 583–611. https://doi.org/10.1146/annurev-genet-120213-092208

Williams, M., Yen, W., Lu, X., Sutherland, A., 2014. Distinct Apical and Basolateral Mechanisms Drive Planar Cell Polarity-Dependent Convergent Extension of the Mouse Neural Plate. Dev. Cell 29, 34–46. https://doi.org/10.1016/j.devcel.2014.02.007

Wisniewski, E.O., Mistriotis, P., Bera, K., Law, R.A., Zhang, J., Nikolic, M., Weiger, M., Parlani, M., Tuntithavornwat, S., Afthinos, A., Zhao, R., Wirtz, D., Kalab, P., Scarcelli, G., Friedl, P., Konstantopoulos, K., 2020. Dorsoventral polarity directs cell responses to migration track geometries. Sci. Adv. 6, eaba6505. https://doi.org/10.1126/sciadv.aba6505

Wu, P.-J., Kabakova, I.V., Ruberti, J.W., Sherwood, J.M., Dunlop, I.E., Paterson, C., Török, P., Overby, D.R., 2018. Water content, not stiffness, dominates Brillouin spectroscopy measurements in hydrated materials. Nat. Methods 15, 561–562. https://doi.org/10.1038/s41592-018-0076-1

Zhang, J., Alisafaei, F., Nikolić, M., Nou, X.A., Kim, H., Shenoy, V.B., Scarcelli, G., 2020. Nuclear Mechanics within Intact Cells Is Regulated by Cytoskeletal Network and Internal Nanostructures. Small 16, 1907688. https://doi.org/10.1002/smll.201907688

Zhang, J., Raghunathan, R., Rippy, J., Wu, C., Finnell, R.H., Larin, K.V., Scarcelli, G., 2019. Tissue biomechanics during cranial neural tube closure measured by Brillouin microscopy and optical coherence tomography. Birth Defects Res. 111, 991–998. https://doi.org/10.1002/bdr2.1389

Zhang, J., Scarcelli, G., 2021. Mapping mechanical properties of biological materials via an add-on Brillouin module to confocal microscopes. Nat. Protoc. 16, 1251–1275. https://doi.org/10.1038/s41596-020-00457-2

Zhou, J., Kim, H.Y., Davidson, L.A., 2009. Actomyosin stiffens the vertebrate embryo during crucial stages of elongation and neural tube closure. Development 136, 677–688. https://doi.org/10.1242/dev.026211

Zhou, J., Pal, S., Maiti, S., Davidson, L.A., 2015. Force production and mechanical accommodation during convergent extension. Development 142, 692–701. https://doi.org/10.1242/dev.116533